In compliance with the
Canadian Privacy Legislation
some supporting forms
may have been removed from
this dissertation.

While these forms may be included
in the document page count,
their removal does not represent
any loss of content from the dissertation.

University of Alberta

Characterization of rare-earth titanium antimonides

by

Sydney Henry Devon Moore

A thesis submitted to the Faculty of Graduate Studies and Research in partial fulfillment of the requirements for the degree of Master of Science

Department of Chemistry

Edmonton, Alberta

Fall 2003

National Library
of Canada

Acquisitions and
Bibliographic Services

395 Wellington Street
Ottawa ON K1A 0N4
Canada

Bibliothèque nationale
du Canada

Acquisisitons et
services bibliographiques

395, rue Wellington
Ottawa ON K1A 0N4
Canada

Your file Votre référence
ISBN: 0-612-87841-4
Our file Notre référence
ISBN: 0-612-87841-4

The author has granted a non-exclusive licence allowing the National Library of Canada to reproduce, loan, distribute or sell copies of this thesis in microform, paper or electronic formats.

L'auteur a accordé une licence non exclusive permettant à la Bibliothèque nationale du Canada de reproduire, prêter, distribuer ou vendre des copies de cette thèse sous la forme de microfiche/film, de reproduction sur papier ou sur format électronique.

The author retains ownership of the copyright in this thesis. Neither the thesis nor substantial extracts from it may be printed or otherwise reproduced without the author's permission.

L'auteur conserve la propriété du droit d'auteur qui protège cette thèse. Ni la thèse ni des extraits substantiels de celle-ci ne doivent être imprimés ou aturement reproduits sans son autorisation.

Canada

University of Alberta

Library Release Form

Name of Author: Sidney Henry Devon Moore

Title of Thesis: Characterization of rare-earth titanium antimonides

Degree: Master of Science

Year this Degree Granted: 2003

Permission is hereby granted to the University of Alberta Library to reproduce single copies of this thesis and to lend or sell such copies for private, scholarly or scientific research purposes only.

The author reserves all other publication and other rights in association with the copyright in the thesis, and except as herein before provided, neither the thesis nor any substantial portion thereof may be printed or otherwise reproduced in any material form whatever without the author's prior written permission.

May 6, 2003

University of Alberta

Faculty of Graduate Studies and Research

The undersigned certify that they have read, and recommend to the Faculty of Graduate Studies and Research for acceptance, a *thesis Characterization of rare-earth titanium antimonides* submitted by S. H. Devon Moore in partial fulfillment of the requirements for the degree of Master of Science.

Prof. A. Mar

Prof. R. G. Cavell

Prof. K. Chow

April 30, 2003

Abstract

The members of rare-earth antimonide family RE_3TiSb_5 (RE = La, Ce, Pr, Nd, Sm) were synthesized through reactions of the elements and characterized by X-ray diffraction. The electronic and magnetic properties of the La, Ce, Pr, Nd, and Sm members were investigated. These compounds possess low-dimensional features that are manifested as isolated linear antimony chains and $TiSb_{6/2}$ face sharing octahedra. Extended Hückel band structure calculations were performed to determine if the observed trends in electrical behavior could be rationalized by the respective band structures.

A new family of rare-earth titanium antimonides, $RETi_3(Sn_xSb_{1-x})_4$ (RE = Nd, Sm), was serendipitously discovered through reactions of the elements. The crystal structure of both members was determined, and comprises layers of face and edge sharing $TiSb_{4/6}Sb_{2/3}$ octahedral, with rare earth atoms occupying depressions on the layer. The range of tin content was explored, as was the potential for expanding the family to include other rare earths.

To those who have come before;
To those who follow

Acknowledgments

I wish to thank my supervisor, Dr. Arthur Mar, for accepting me into his group and for the wonderful projects for my thesis. I also thank Dr. Laura Deakin for both her support and for helping to push me up the learning cliff of magnetism. My thanks also go to the previous graduate students in the Mar group: Dr. Allison Mills and Dr. Meitian Wang for their assistance in helping me start off. I wish to thank my contemporary, Shane Crerar. Without his unique perspective and equally cromulent sense of humor I would have been terribly bored and would never have been introduced to *Invader Zim*. I have had the privilege of working with several undergraduate students (Chad Lewis, Chris Sheets, Mark Morgan, Craig Muirhead, Grace Chan, and Joleen Ostashek) during their summer work terms and 401/403 projects.

My thanks go to Dr. Robert McDonald and Dr. Mike Ferguson (Structure Determination Laboratory) for the collection of single crystal X-ray data for us. Their door was always open to me for discussion about practically anything. My thanks also go to Tina Barker and George Braybrook for the EDX analyses. To Tina, who tirelessly worked through hundreds of samples and promptly delivered the results to us. To George, who was always accommodating to us when we appeared without an appointment.

I would like to thank Dr. Jason Cooke for assisting me during my time as a T.A. I found our conversations both enlightening and helpful. Thanks to Dr. J. Takats, Dr. B Jordan and Dr. J Veinot who were marvelous professors to for whom to T.A..

I wish to acknowledge the excellent work of the support staff, whom have been professional in their deportment and in the execution of their responsibilities. They

helped to make the department here pleasant and were great fun to interact with. My thanks to Jackie Jorgensen(4th floor secretary), Ed Feschuk (Electronics), Bernie (Stores), Tyler (Stores), Andrew (Stores), Ken Jorgenson (Stores) , Jennett (Main office secretary), Elona Baker (Grad secretary), the caretakers Mo and Emily, Steve and Nick (Liquid Helium Techs.).

I have tried to focus of my work during my time in Alberta, but thanks to the effort of several good people I have been unable to remain hidden in the lab. My thanks go to Dr. Jim Dennett for his suggestion that I take up campus recreational soccer. At the time I was afraid it would be to detrimental on my research. In retrospect it was well worth the time I devoted to it and I know that I came away with so very much more then I had when I started.

Table of Contents

Chapter 1: Introduction 1

Introduction 1

Synthesis 2

Characterization 3

Physical Properties of Solids 6

Physical properties measurement System 13

Low-dimensional intermetallics and Antimonides 14

References 25

Chapter 2: Physical properties and bonding in RE_3TiSb_5 (*RE* = La, Ce, Pr, Nd, Sm): 27

Introduction 27

Experimental Section 29

Synthesis 29

Structure determination 29

Transport measurements 30

Magnetic measurements 30

Band Structure 31

Results and Discussion 32

Structure 32

Transport Properties 32

Magnetism and Magnetoresistance 33

Band structure 35

Conclusion 38

References 53

Chapter 3: New layered *RE*Ti($Sn_{0.1}Sb_{0.9}$)$_4$ (*RE* = La, Ce, Pr, Nd, Sm): Crystal Structures of NdTi($Sn_{0.1}Sb_{0.9}$)$_4$ and SmTi($Sn_{0.1}Sb_{0.9}$)$_4$ 55

Introduction 55

Experimental Section 57

Synthesis 57

Structure Determination 58

Discussion 60

Synthesis 60

Structure 60

Conclusions 63

References 79

Chapter 4: Conclusion 81

Future Directions 83

Appendix 86

List of Tables

Table 1–1. Summary of recent ICSD search for rare-earth transition-metal antimonides 17

Table 2–1. Crystallographic Data for RE_3TiSb_5 (RE = Ce, Pr, Nd, Sm) 40

Table 2–2. Positional and Equivalent Isotropic Displacement Parameters for RE_3TiSb_5 (RE = Ce, Pr, Nd, Sm) 41

Table 2–3. Selected Interatomic Distances (Å) in RE_3TiSb_5 (RE = La, Ce, Pr, Nd, Sm) 42

Table 2–4. Extended Hückel Parameters 43

Table 2–5. Summary of Resistivity and Magnetism Data for RE_3TiSb_5 44

Table 2–6. Mulliken charges and integrated overlap populations for $[TiSb_5]^{9-}$ substructure in RE_3TiSb_5 45

Table 3–1. Reaction conditions and results of exploratory $RETi_3Sb_4$ (RE = La, Ce, Pr, Nd, Sm, Gd) reactions. Where indicated as a product, the $RETi_3Sb_4$ phase was detected at low yields (~5%). 65

Table 3–2. Crystallographic data for $NdTi_3(Sn_{0.1}Sb_{0.9})_4$ and $SmTi_3(Sn_{0.1}Sb_{0.9})_4$ 66

Table 3–3. Positional and equivalent isotropic displacement parameters for $RETi_3(Sn_{0.1}Sb_{0.9})_4$ RE = Nd, Sm 68

Table 3–4. Selected interatomic distances (Å) for $RETi_3(Sn_{0.1}Sb_{0.9})_4$ (RE = Nd, Sm) 69

Table 3–5. Refined cell parameters for observed $RETi_3Sb_4$ phases 70

Table 3–6. Comparison of interatomic distances (Å) in Ti–Sb phases 71

Table A–1. Anisotropic displacement parameters (Å^2) for Ce_3TiSb_5, Pr_3TiSb_5, Nd_3TiSb_5 and Sm_3TiSb_5 for data collections at 22 °C 86

Table A–2. Anisotropic displacement parameters (Å^2) for $NdTi_3X_4$ and $SmTi_3X_4$ (X = $Sn_{0.1}Sb_{0.9}$) for data collections at 22°C 87

Table A–3. X-ray powder diffraction data for trial 1 $LaTi_3Sb_4$ 88

Table A–4. X-ray powder diffraction data for trial 3 $LaTi_3Sb_4$ 89

Table A–5. X-ray powder diffraction data for trial 1 $CeTi_3Sb_4$ 90

Table A–6. X-ray powder diffraction data for trial 3 $CeTi_3Sb_4$ 91

Table A–7. X-ray powder diffraction data for trial 1$PrTi_3Sb_4$ 92

Table A–8. X-ray powder diffraction data for trial 1 $NdTi_3Sb_4$ 93

Table A–9. X-ray powder diffraction data for trial 6 $SmTi_3Sb_4$.....94

Table A–10. X-ray powder diffraction data for trial 6 $SmTi_3(Sn_{0.2}Sb_{0.8})_4$.....95

List of Figures

Figure 1–1. Basics of a XRD experiment. 18

Figure 1–2. General relationship between resistivity and temperature for insulators, semiconductors and metals 19

Figure 1–3. Hypothetical plot of resistivity vs temperature showing a superconducting transition from ρ_0, and the expected effect of an applied field. As the applied field is incrementally increased, the transition temperature is depressed. Here T_C is defined as when ρ falls to 90% of ρ_0 20

Figure 1–4. Origin of metallic band structure arising from atomic orbital overlap orbital interactions 21

Figure 1–5. Hypothetical isothermal magnetisation versus coercive field of (a) a type I superconductor and (b) a type II superconductor 22

Figure 1–6. Hypothetical plot of ac susceptibility of a superconducting transition without an applied field and the expected effect of an applied field. As the applied field is increased the critical temperature is depressed. Here T_C is defined as 90% of the signal prior to the transition 23

Figure 1–7. Layout of a four probe experiment used to determine resistivity 24

Figure 2–1. Structure of RE_3TiSb_5 (*RE* = La, Ce, Pr, Nd, Sm) viewed down the *c* axis. The large lightly shaded circles are *RE* atoms, the small solid circles are Ti atoms, and the medium open circles are Sb atoms 46

Figure 2–2. Zero-field electrical resistivity of single crystals of RE_3TiSb_5 (*RE* = (a) La, (b) Ce, (c) Pr, (d) Nd, (e) Sm) measured along the *c* axis between 2 and 300 K. Insets show low-temperature behaviour 47

Figure 2–3. (a) Field dependent single-crystal electrical resistivity, (b) temperature dependence of zero-field-cooled ac magnetic susceptibility under various applied fields (and an additional field-cooled run at 200 Oe), and (c) isothermal magnetization at 2 K for La_3TiSb_5. Lines shown are included only to guide the eye 48

Figure 2–4. (a) Field dependent single-crystal electrical resistivity, (b) temperature dependence of zero-field-cooled ac magnetic susceptibility under various applied fields (and an additional field-cooled run at 200 Oe), and (c) isothermal magnetization at 2 K for Ce_3TiSb_5. Lines shown are included only to guide the eye 49

Figure 2–5. Field dependent single-crystal electrical resistivity for Nd_3TiSb_5 50

Figure 2–6. Magnetic susceptibility (M/H) of Sm_3TiSb_5 under an applied field of 1.0 T. 51

Figure 2–7. Band dispersion curves along special symmetry lines for the $[TiSb_5]^{9-}$ substructure in La_3TiSb_5. The dashed horizontal line marks the Fermi level (ε_f = –8.71 eV). A representation of the hexagonal Brillouin zone is shown with the irreducible wedge outlined 52

Figure 2–8. (a) Density of states (DOS) (with the Ti projection shown by the filled area; what remains of the DOS is the Sb projection) and crystal orbital overlap population (COOP) curves for the (b) Ti–Sb, (c) Sb–Sb, and (d) Ti–Ti contacts in the $[TiSb_5]^{9-}$ substructure in La_3TiSb_5. The dashed horizontal line marks the Fermi level (ε_f = –8.71 eV) 53

Figure 3–1. Structure of $RETi_3(X)_4$ (RE= Nd, Sm; $X = Sn_{0.1}Sb_{0.9}$) viewed down [100]. The large shaded circles are RE atoms, the small solid circles are Ti atoms, and the open circles represent $Sn_{0.1}Sb_{0.9}$ 72

Figure 3–2. Plot of unit cell volumes vs RE 73

Figure 3–3. (a) type 1 octahedron, (b) type 2 octahedron. Small dark circles are Ti atoms, circles with horizontal hachure are X(1), open circles with thick rims are X(2) and the open circles are X(3) 74

Figure 3–4. Six $TiSb_{4/6}Sb_{2/3}$ octahedra forming a pseudohexagonal arrangement. The solid black circles are the Ti atoms, circles with horizontal hachure are $X(1)$, open circles with thick rims are $X(2)$ and the open circles are $X(3)$ 75

Figure 3–5. Coordination environment of the RE atom in $RETi_3(Sn_{0.1}Sb_{0.9})_4$ (RE = Nd, Sm). Circles with horizontal hachure are $X(1)$ and open circles with thick rims are $X(2)$ 76

Figure 3–6. Comparison of (a) $RECrSb_3$ and (b) $RETi_3(Sn_{0.1}Sb_{0.9})_4$ (RE= Nd, Sm). Large shaded circles are RE atoms, the small solid circles are M atoms (M = Cr, Ti), and the open circles are Sb or Sn atoms 77

Figure 3–7. Arrangement of Ti atoms in $NdTi_3(Sn_{0.1}Sb_{0.9})_4$. The Ti(1) and Ti(2) inter layer distances for $SmTi_3(Sn_{0.1}Sb_{0.9})_4$ are 4.455 (2) Å and 4.629 (2) Å respectively. Ti(2) centers are indicated in (a), all other centers are Ti(1) 78

Figure 4–1. Hypothetical transformation of $RETi_3X_4$ phase to the RE_3TiSb_5 phase. X = $Sn_{0.1}Sb_{0.9}$. Large shaded circles are RE atoms, the small solid circles are Ti atoms and the open circles are Sb or Sn atoms 85

List of Abbreviations and Symbols

ac	alternating current
anal.	analysis
arb. units	arbitrary units
B	magnetic induction
χ	magnetic susceptibility
C	Celsius
C	Curie constant
calcd	calculated
COOP	crystal orbital overlap population
DOS	density of states
ε_f	Fermi level
EDX	energy dispersive X-ray
emu	electromagnetic unit
eV	electron volt
f.u.	formula unit
H	magnetic field strength
Hz	hertz
I	current
k	Boltzmann's constant
K	Kelvin
M	magnetization
μ_B	Bohr magneton
μ_{eff}	effective magnetic moment
μ_{sat}	saturation magnetic moment
N_A	Avogadro's number
Oe	oersted
ρ	electrical resistivity
σ	electrical conductivity
θ	Weiss temperature
T	temperature
T	tesla
Ω	ohm

List of Crystallographic Abbreviations and Symbols

a, b, c	lengths of basis vectors, lengths of cell edges
a^*, b^*, c^*	lengths of reciprocal basis vectors, lengths of reciprocal cell edges
α, β, γ	interaxial (lattice) angles between b and c, a and c, and a and b axes, respectively
$\alpha^*, \beta^*, \gamma^*$	interaxial (lattice) angles between b^* and c^*, a^* and c^*, and a^* and b^* axes, respectively
Å	angström
d_{hkl}	interplanar distance, or spacing, of neighboring net planes (hkl)
F_c	calculated structure factor
F_o	observed structure factor
hkl	indices of the Bragg reflection (Laue indices) from the set of parallel equidistant net planes (hkl)
(hkl)	indices of a crystal face, or of a single net plane (Miller indices)
[hkl]	indices of a lattice direction
λ	wavelength
μ	linear absorption coefficient
P	experimental instability factor in weighting scheme (used in the calculation of $\sigma(I)$ to downweight intense reflections)
R	residual index
R_w	weighted residual index
R_{int}	residual index for averaged symmetry equivalent reflections
ρ_{calc}	calculated density
σ	standard deviation
U_{eq}	equivalent isotropic atomic displacement parameter
U_{ij}	elements of anisotropic atomic displacement parameter tensor

List of Crystallographic Abbreviations and Symbols (continued)

V	cell volume of the direct lattice
w	weighting factor applied to structure factor
Z	number of formula units per unit cell

Chapter 1

Introduction

Solid-state chemistry is an established field of research that is experiencing a period of intense growth. Newly discovered substances such as quasi-crystals have challenged long-held fundamental ideas, while others, such as thermoelectrics, hold promise for new technologies. Part of the reason why this field has developed so quickly is its strong interdisciplinary nature. Advances in one field help to stimulate those in another, whether it is through new synthetic techniques, new compounds, or simply new ideas.

By examining compounds and their properties, solid-state chemistry attempts to determine the relationship with composition and structure. Insight gained from this research aids in understanding the underlying phenomena giving rise to specific properties and in turn may lead to the successful design of new compounds with specific properties. However, the main synthetic challenge is not of exploration but of technique. Many compounds require specific non-intuitive conditions in order to form. This can make exploratory efforts difficult because of the number of variables that need to be controlled and systematically altered. It is for this reason that solid-state synthesis is not as predictable as other kinds of synthetic chemistry.

Synthesis

Reactions between solids present two major synthetic challenges to overcome. The largest obstacle is the slow reaction rate due to slow reagent mobility. The major transport method for a solid-solid reaction is slow diffusion, dependent largely on the temperature. The second setback is that the product typically forms at the interface of the reagents, such as an oxide layer on the surface of a metal. This effectively terminates the reaction by isolating the reagents from each other. These two difficulties are overcome in practice by using finely powdered reagents and high reaction temperatures (above 500 °C). With the increased surface area of a powder, more of the reagents can react, and the elevated temperature causes the reactants to diffuse faster. A common practice is to repeatedly grind up a product, re-press it into a pellet and then reheat it until the reaction yield is satisfactory.

Alternatively a flux, which is essentially a solvent for high temperature reactions, may be used to improve the rate of a reaction and aid the growth of crystals. Criteria for a flux are similar to a solvent in molecular chemistry; it must be non-reactive towards the reagents and product as well as being separable from the product. An example of a common flux is elemental tin. With a melting point of 231 °C it is liquid at typical reaction temperatures and may be removed from the products with 6M hydrochloric acid. Additionally the reaction vessel may be placed in a centrifuge and spun while the tin is molten, which can remove a sizable portion of tin from the reaction bulk.

Arc melting reaction is a synthetic technique that overcomes the aforementioned difficulties without a flux. This method uses the intense heat from an electric arc (under an inert atmosphere), which is enough to melt most elements allowing them to react in a

molten state overcoming slow reaction rates. Although this method is fast (~30 seconds) and frequently successful, it does have drawbacks. The heat from the arc is so intense that it can partially vaporize reagents, resulting in the incorrect stoichiometry. By starting with an excess (about 5%) of the volatile reagent, an approximate reaction stoichiometry can be maintained. Another disadvantage of this technique is that the rapid cooling disfavours the formation of large crystals and powders. Annealing the arc-melted product is common and may serve to produce crystals suitably sized for characterization.

Characterization

Compound characterization is crucial in any field of synthetic chemistry and can be achieved using a variety of techniques. Intermetallic materials do not yield to some of the more typical characterization methods such as solution NMR, FT-IR or combustion elemental analysis; instead, there is a variety of other structural and electronic characterization techniques available.

Elemental analysis.[1] Scanning Electron Microscopy (SEM) is an imaging technique that offers a qualitative assessment of a crystal's habit, potentially revealing information about its symmetry. The sample is bombarded with electrons sourced from a tungsten filament, accelerated through a potential and focused by several magnetic lenses to a point. The point is directed over the sample area incrementally, in a process called rastering. The bombarding electrons knock core electrons from the surface atoms in the sample, which are then detected and converted to a signal. The more electrons there are in the target area, the more electrons get ejected and the stronger the signal. Point by point, an image is constructed and displayed on a cathode ray tube. Energy Dispersive X-ray (EDX) analysis is a method performed on a properly equipped SEM that

determines the presence of elements based on X-ray emission profiles. When outer shell electrons fall into the holes left by the ejected electrons, the atoms emit X-rays with characteristic energies, which allow elemental determination. Intensity analysis of the X-rays is semi-quantitative, allowing for an approximation of the relative amounts of each element present.

Crystallography. The structure of crystalline solids can be determined by analyzing their X-ray diffraction patterns. Although the diffraction arises from the interaction of the electrons in the crystal with the X-rays, it is convenient to model this phenomenon as the reflection of X-rays from planes in the crystal. Bragg's law, Equation 1–1, shows that only at certain angles, θ, will the X-rays interfere constructively and propagate from the crystal. The interplanar spacing, denoted by d_{hkl}, can be calculated with Equation 1–1 by using a known wavelength, λ, of radiation and measuring its angle of diffraction. The theoretical planes are identified by indices (*hkl*) to distinguish them

$$n\lambda = 2d_{hkl}\sin(\theta) \qquad \textbf{Equation 1–1}$$

Equation 1–2

$$d_{hkl}^{-1} = \sqrt{h^2a^{*2} + k^2b^{*2} + l^2c^{*2} + hka^*b^*2\cos\gamma^* + hla^*c^*2\cos\beta^* + klb^*c^*2\cos\alpha^*}$$

and the distance between is related to the reciprocal unit cell parameters (a^*, b^*, c^*, α^*, β^*, γ^*) by Equation 1–2, which simplifies to Equation 1-3 for an orthorhombic system.[2] The symmetry of the collected pattern reveals information about the internal symmetry of

$$\frac{1}{d_{hkl}} = \left(h^2a^{*2} + k^2b^{*2} + l^2c^{*2}\right)^{1/2} \qquad \textbf{Equation 1–3}$$

the crystal, while the intensity of the pattern contains information about the atomic positions.

The essentials of the procedure to collect the diffraction pattern of a single crystal is to direct collimated monochromatic X-rays at the crystal and to record both the angle of reflection and the intensity of the scattered X-rays. Classically the information was recorded with film and photomultiplier tubes, but more modern instruments utilize a CCD detector to record the information digitally. The information is then manipulated electronically with the aid of software packages such as SHELXTL to determine the structure of the crystal, making the processes much more automated.[3] Despite the near "black box" nature of the process, structure solution does have pitfalls and requires the attention of a competent chemist.

When single crystals are unavailable, X-ray powder diffraction (XRD) is useful to determine the identity of crystalline compounds present and their relative amounts in a sample. A drawback of this method is that amorphous phases cannot be detected. Because the diffraction pattern of a given crystal is unique, it can be used as a fingerprint to identify the presence of a particular crystalline phase. From the powder pattern of a reaction product, it is possible to identify all the known crystalline phases and estimate their relative abundance,[4] to within +/- 5%. Because a product consists of many crystallites randomly oriented with respect to the incident X-ray beam, the diffraction pattern is made up of lines instead of single spots. Figure 1–1 shows how a crystal's orientation can satisfy Bragg's law and have a random orientation along one axis.

If a known phase is present, its diffraction pattern may be indexed and its cell parameters determined. Each line corresponds to a reflection from a lattice plane in the

crystal. Using Equation 1–1, d_{hkl} may be calculated and using the relationship described in Equation 1–3, cell parameters can be determined through an iterative process.

A Guinier camera is a device that collects X-ray powder diffraction information on film. This technique is still popular because it uses a geometric principle that focuses the diffracted X-rays making the film data very sharp and intense. Because of this advantage, the method is still employed today by careful solid state chemists.

Physical Properties

Electrical conductivity.[4,5,6] A measure of the capacity for the conduction of charge carriers under an applied voltage is quantified by a material's conductivity, σ. The conductivity is described by Equation 1–4, where n is the number of charge carriers (electrons), |e| is the magnitude of the charge on the carriers, and μ is their mobility through the material. The mobility of carriers in a metal is very strongly influenced by temperature. The inverse quantity resistivity, ρ, is defined in Equation 1–5. Resistivity is more commonly used in describing transport behaviour in metals because it generally varies linearly with temperature. A material is classified into one of three groups based on how its resistivity varies with temperature as shown in Figure 1–2.

$$\sigma = n|e|\mu \qquad \textbf{Equation 1–4}$$

$$\sigma \equiv \frac{1}{\rho} \qquad \textbf{Equation 1–5}$$

The linear temperature dependence of a metal's resistivity arises from the scattering of charge carriers by phonons, which are quantized lattice vibrations. As the temperature is decreased, vibrational motion is diminished, so that the resistivity

decreases. At very low temperatures, electron-phonon scattering is minimized and the scattering now becomes dependent on impurities and defects in the material. Because the concentration of these defects and impurities is constant with respect to temperature, the metal's resistivity becomes temperature-independent at low temperatures. A simple expression of the resistivity of a metal is given in Equation 1–6.

$$\rho(T) = \rho_0 + \rho_{\substack{phonon- \\ electron \\ scattering}}(T) \qquad \textbf{Equation 1–6}$$

Other variables may affect resistivity. For example, the conduction electrons may also scatter off magnetic moments; if these magnetic moments attain long-range order, the resistivity decreases due to a loss of spin-disorder scattering. More dramatically, the material may form a superconducting phase and the resistivity may vanish below a critical temperature, T_C. The resistivity of a superconductor is shown in Figure 1–3. Application of an external magnetic field can depress T_C, destroying the superconducting phase completely above a critical field, H_C. Superconductors may only carry a finite amount of current. If the current flowing through the sample exceeds a critical current, I_C, the superconducting state will be disrupted.

The classical example of a conductor is a metal; metals are characterized in part by their low resistivity. The low resistivity is attributed to the large number of charge carriers that are delocalised throughout the structure. Molecular Orbital (M.O.) theory demonstrates that when two atomic orbitals of the same energy are combined, two molecular orbitals of different energies are produced: an antibonding combination that is high in energy and a bonding combination that is low. If this is extended to four atomic orbitals, then two bonding and two antibonding molecular orbitals result as depicted in

Figure 1–4. Generally it can be observed that the spacing between energy levels becomes smaller as the number of the atomic orbitals increases. When this is extended to a sufficiently large number of orbitals the result is a virtual continuum of possible energy levels, or a band, with no gap between the bonding and antibonding states. The level up to which electrons fill the band depends on the number of electrons in the initial atomic orbitals. The Fermi level is the energy level below which all electrons reside at 0 K. At higher temperatures the thermal energy is sufficient to promote electrons above the Fermi level, while generating holes below it. The number of charge carriers in a metal is due then to the band nature of the electron energy levels.

Insulators are materials where there is a discontinuity in the energy levels above the Fermi level, resulting in a range of forbidden energy states called a band gap. The region below the gap is called the valence band (VB), the region above (generally) is called the conduction band (CB). The gap between the CB and the VB is large enough to prevent electrons from crossing the gap unless they have significant amounts of energy. Semiconductors are so named because their band gap is large enough to prevent electrons below a certain energy level from being promoted to the conduction band, limiting the number of carriers in the material, which decreases the conductivity. As the temperature of a semiconductor is increased, the resistivity decreases as more electrons are thermally promoted to the CB; the reverse is true upon cooling as shown in Figure 1–2.

Magnetism.[4,5,7,8] Macroscopic magnetic properties originate from the spins of electrons. When an external magnetic field H is applied, a magnetisation M develops to result in the magnetic induction B in a sample (Equation 1–7). The magnetization may be viewed as the sum of all the individual magnetic moments in the sample.

$$B = H + 4\pi M$$ **Equation 1–7**

When there is no long-range order, magnetic behaviour can be divided into two categories based on the magnetization: $|M| > 0$ (paramagnetic) and $|M| < 0$ (diamagnetic). Magnetic susceptibility, χ, is defined in Equation 1–8, and is diagnostic of different types of magnetic behaviour.

$$\chi = \frac{M}{H}$$ **Equation 1–8**

Paramagnetism. All paramagnetic materials contain unpaired electrons, which possess a magnetic moment arising from their orbital motion and spin. The spins are randomly oriented in the absence of an applied magnetic field. However, in the presence of an external magnetic field, the individual magnetic moments align preferentially along the direction of the applied field, and $|M| > 0$; therefore χ will be positive. The susceptibility for paramagnetic ordering follows the Curie Law, given in Equation 1–9 where T is the temperature and C is the Curie constant of the material. Equation 1–10 defines the Curie constant and shows that it is related to the effective moment (μ_{eff}) of the magnetic centre. In turn μ_{eff} is related to the number of unpaired electrons on the magnetic centre.

$$\chi = \frac{C}{T}$$ **Equation 1–9 Curie Law**

$$C = \frac{N_A \mu_{eff}^{\ 2}}{3k}$$ **Equation 1–10 Curie constant**

Ferromagnetism. If long-range ordering occurs and the individual moments couple such that they align with each other, the sample is said to be ferromagnetically ordered, and is referred to as a ferromagnet. For a ferromagnetically ordered material, the susceptibility is positive, dependent on H and T. Each ferromagnetic material has a characteristic critical temperature (T_C) above which the moments are paramagnetically ordered. This results from thermal energy sufficient to prevent the moments from ordering. The susceptibility of a ferromagnet does not follow the Curie law. Instead it is modeled by the Curie-Weiss law given in Equation 1–11 where Θ is called the Weiss temperature and is equal to T_C of the ferromagnet. Below T_C the moments form *domains*, which are regions of mutually aligned spins. Each domain has a magnetic moment associated with it proportional to the number of spins encompassed within it. The field dependence of a ferromagnet is due to the behaviour of the domains with increasing or deceasing H: as the H increases, the domains coalesce and M increases until it reaches a maximum value called the saturation magnetization, M_{sat}. Upon decreasing H, the domains re-establish themselves. When H has been completely removed, there remains a remanent magnetization, M_{rem} as some of the domains remain coalesced.

$$\chi = \frac{C}{T - \Theta} \qquad \textbf{Equation 1–11 Curie-Weiss Law}$$

Antiferromagnetism. If the coupling of the moments is such that neighbouring moments are aligned anti-parallel, then the material is referred to as an antiferromagnet. The susceptibility of an antiferromagnet is positive, dependent on the temperature and may be dependent of H. Antiferromagnets also follow the Curie-Weiss law, except in this case Θ is equal to the Néel temperature (T_N). The Néel temperature is a

characteristic temperature for an antiferromagnet about which the magnetic profile changes. Above T_N, the material is typically paramagnetic, while below it is antiferromagnetically ordered; the temperature dependence arises from the same source as with ferromagnets.

Diamagnetism. This is by far the most common magnetic behaviour simply because it is present in all matter with paired electrons, including any inner shell electrons. An electron pair creates a weak magnetic moment, which aligns against the external magnetic field, resulting with $B > H$, and the material's magnetisation negative. The susceptibility is negative, and both T and H independent. The effect is weak (approximately 1000 times weaker then the paramagnetic effect) and can be difficult to measure.

Pauli paramagnetism. The magnetism of a non-ferromagnetic metal does not fall into any one of the above categories owing to the itinerant nature of the electrons. The susceptibility is positive suggesting paramagnetism, but on average ~100 times weaker then the typical paramagnetic effect. Conversely it is temperature independent, which is characteristic of diamagnetism. The origin of the behaviour is not the localized moments of localized electrons, but rather the moment of *delocalised* electrons near the Fermi level. An external magnetic field perturbs the electrons in the bands. Electron pairs at the Fermi level separate and one of the electrons is promoted to the next energy level. This generates a large number of unpaired electrons, which behave similarly to a paramagnetically ordered material. This type of magnetism is known as Pauli paramagnetism and is common in metals.

Superconductivity. Superconductivity is a distinct phenomenon observable by both electrical and magnetic experiments. The name comes from the observed loss of resistance below a specific temperature with the dissipation-less flow of an electrical current. Since its discovery over 94 years ago there has been great interest in describing the phenomenon from a theoretical point of view.[9] Although these efforts have not been entirely successful, there is still no all-encompassing explanation of superconductivity. Experimentally the susceptibility of a superconductor is negative and independent of H, as with diamagnetism, but the magnitude of the effect is greater. A theatrical demonstration of the extent of the diamagnetic behaviour is of a magnet floating over a superconductor (or vice versa). Known as the *Meissner effect*, this demonstrates the *total* exclusion of an external magnetic field from the superconductor, preventing the magnet from approaching it. Theoretically the internal magnetic flux is zero ($|B| = 0$). If $|B| = 0$ then, by Equations 1–7 and 1–8, $|M|$ must be equal to $-|H|/4\pi$, and χ equal to $-1/4\pi$. The Meissner effect may be quantified through magnetic measurements. If a superconducting sample's isothermal magnetisation is measured and plotted against an increasing applied magnetic field, the plot may look like either Figure 1–5(a) or Figure 1–5(b). These two plots describe the behaviour of type I and type II superconductors, respectively. With a type I superconductor, the superconducting state exists until a critical field value (H_C) is reached, at which point the state collapses. Until that point the slope is linear and equal to $-1/4\pi$. In a type II superconductor the magnetisation is also negative and linear with respect to H until H_{C1} after which the magnitude decays until it reaches 0; the field at which this happens is H_{C2}. The behaviour between H_{C1} and H_{C2} arises from the

penetration of the external field lines into the material, creating discrete regions of non-superconducting behaviour.

This effect may also be seen in the ac susceptibility (χ_{ac}) measurements, an example of which is shown in Figure 1–6. These measurements employ an alternating external magnetic field and the susceptibilities are measured with varying temperature. If a static external magnetic field is applied, the critical temperature of the state is depressed.

Physical Properties Measurement System

Although by no means a universal laboratory instrument, mention must be given to Quantum Design's Physical Properties Measurement System (PPMS). The PPMS has a modular nature that allows it to perform a large number of experiments. The computer-control allows for reproducible experimental conditions. The basic procedure for both magnetic measurements and ac transport characterization are described below.

Magnetic measurement. Magnetic samples are typically measured as homogeneous powders, although the PPMS can accommodate thin film samples. During an experiment the sample's magnetic response is determined by inductance methods. The instrument is capable of creating many different magnetic and thermal environments, using dc fields and ac fields over a temperature range of 2–350 K to perform various measurements.

ac transport measurement. The resistivity of a sample is determined by measuring the resistance of the sample. The resistivity is determined through Ohm's Law Equation 1–12, where I is the current between points $I+$ and $I-$ and V is the potential difference between $V+$ and $V-$ as shown in Figure 1–7. The PPMS circuitry holds the

current constant, the potential is measured and the resistance is determined by application of Ohm's law. The dimensions of the sample are input into the software allowing

$$R = \frac{V}{I} \qquad \textbf{Equation 1-12}$$

$$\rho = R\frac{a}{l} \qquad \textbf{Equation 1-13}$$

calculation of the resistivity based on Equation 1–13, where a is the cross-sectional area and l is the distance between the points $V+$ and $V-$.

Low dimensional intermetallics and antimonides.

Low dimensionality in intermetallics is characterised by a directionally specific bond anisotropy throughout the material. Structurally, low dimensionality may manifest itself in different ways. Both of the intermetallics $Ba_4In_8Sb_{16}$[10] and $SrSn_3Sb_4$[11] are low dimensional because they possess "channels" that run along [010]. Other intermetallics possess features such as layers or linear chains. Chains may be heteroatomic as in $Eu_{13}AMnSb_{11}$ (A=Ca, Sr, Ba, Yb),[12] Ba_2NiSi_3[13] or homoatomic as in Ce_3MnBi_5.[14] Layers also may be homoatomic as in CeSbTe[15] or heteroatomic as in $KMnTe_2$.[16] In these low dimensional compounds, novel bonding modes may appear that have analogies in molecular chemistry. The compound Ba_2NiSi_3 contains infinite linear chains of $NiSi_{6/2}$ and has been shown through band structure calculations to be analogous to an infinite metallocene polymer.[13]

Models of bonding within intermetallic compounds that describe structural features and stability have been developed. The classic theory of the structure of metals is based on the closest packing of spheres. Although this theory is adequate for many

simple elemental metals, closest packing rules alone often do not describe the structure in intermetallic compounds. These compounds display atomic arrangements that may require a different model to describe the structure. The Zintl concept attempts to extend electron-counting rules in valence-precise compounds to understanding the bonding in many intermetallic materials. The more electropositive elements are assumed to donate their valence electrons to the more electronegative elements, such that both obtain an octet. If the electronegative elements do not obtain sufficient electrons to achieve their octet configuration, then homoatomic bonding results until their octet is complete. Applying this concept allows for prediction about the bonding in a material based solely on the formula.

The stability of low-dimensional substructures results from the covalent interactions within the anionic-framework. As a consequence of the "infinite" nature of a crystal, the energy levels of the bonds in a substructure form bands, previously discussed in the conductivity section. As a generalization, low-dimensional homoatomic structures are composed essentially of the heavy main-group elements. It is thought this stems from weak s-p orbital mixing, which is prevalent for the heavier elements.[17] Such effects are also thought to affect the stability of a low-dimensional structure against a Peierls distortion. Because antimony is a late main-group element, of low toxicity, cheap and relatively reactive, it is a common element in many low-dimensional intermetallics. The use of rare-earth elements in the synthesis of intermetallic compounds is simply an application of the Zintl concept; the overall structure gains additional stability from ionic interactions between the anionic framework and the cations. The additional presence of magnetic 4f electrons contributes to overall magnetic properties.

Research into ternary rare-earth transition-metal antimonides has proceeded with a bias towards the later transition metals. In 1997, a brief survey by our group of ternary rare-earth transition-metal antimonides showed that there were few examples of ternary rare-earth antimonides containing early transition metals, and none for Ta, Mo, W, Re or Hg.[18] In terms of structural trends, the tendency towards low dimensionality decreases with increasing period and group number. The known ternaries exhibit a variety of properties stemming from different sources. Work by our group focused on the exploring the chemistry of early-transition-metal rare-earth antimonides. During this period, the one-dimensional RE_3MSb$_5$ phase was expanded to include nineteen new members,[19] and the layered REMSb$_3$ (RE = La–Nd, Sm, Gd–Dy, M = V, Cr) phase was discovered.[18,20,21] Preliminary investigation of the series of compounds RE_3TiSb$_5$ (RE = La, Ce, Pr, Nd, Sm) showed metallic behaviour between 50 and 300 K.[22] Band structure calculations used to support the metallic nature of the compounds presented the potential for a superconducting phase. A recent search for new ternary rare earth transition metal antimonides in the ICSD is summarized in Table 1–1, among which are the first examples of compounds with Ir and Rh.[23,24] As with results previous to 1998, the bulk of new compounds are ternaries containing mid- to late-transition metals.

The aim of this thesis is to present the results of the magnetic and ac transport characterisation of the series of compounds RE_3TiSb$_5$ (RE = La, Ce, Pr, Nd, Sm),[25] which confirms the presence of a superconducting phase in two of the compounds. In addition we present the structural characterization of the recently discovered phase RETi$_3$(Sn$_{0.1}$Sb$_{0.9}$)$_4$ (RE = Nd, Sm), along with efforts to date to explore the extent of the Sn–Sb disorder and RE substitution.

Table 1–1. Summary of recent ICSD search for rare-earth transition-metal antimonides

M	Phase	Comments
Ir, Rh [a,23,24]	*REM*Sb	XRD data only
Rh [a,25]	$RE_{0.1}M_8Sb_{24}$	Single crystal
Mn[27]	$RE_{14}MSb_{11}$	Single crystal, ferromagnets
Pd, Ni[28]	RE_5M_2Sb	XRD data only
Fe[29]	$RE_{0.8}M_4Sb_{12}$	XRD data only, ferrimagnet
Pt[30]	$RE_3M_7Sb_4$	Single crystal

[a] The Ir and Rh ternaries are significant as they represent the first such example for those elements.

$$n\lambda = 2d_{hkl}\sin(\theta)$$

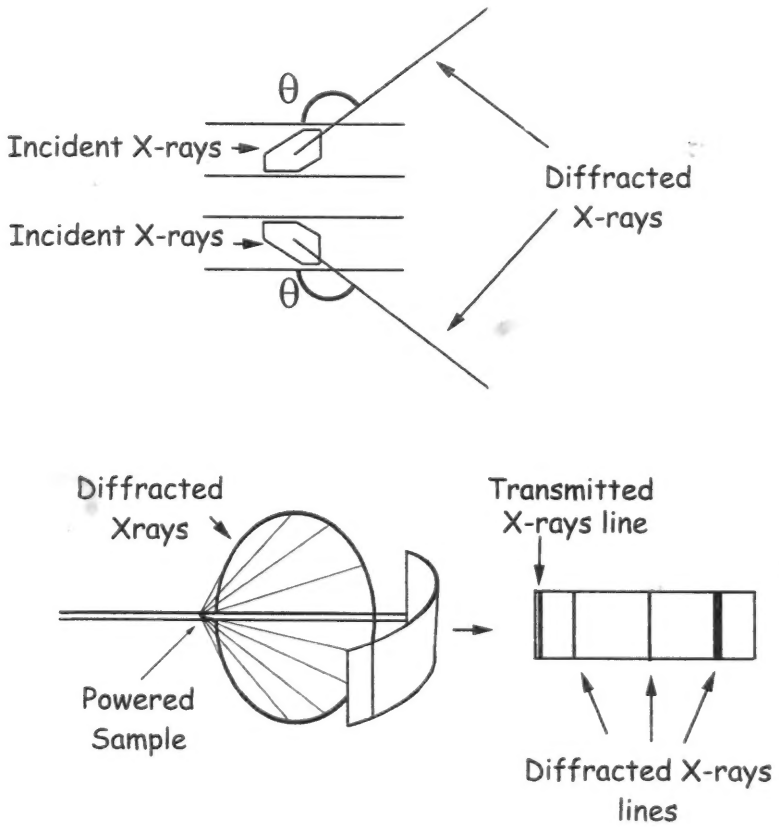

Figure 1–1. Basics of a XRD experiment.

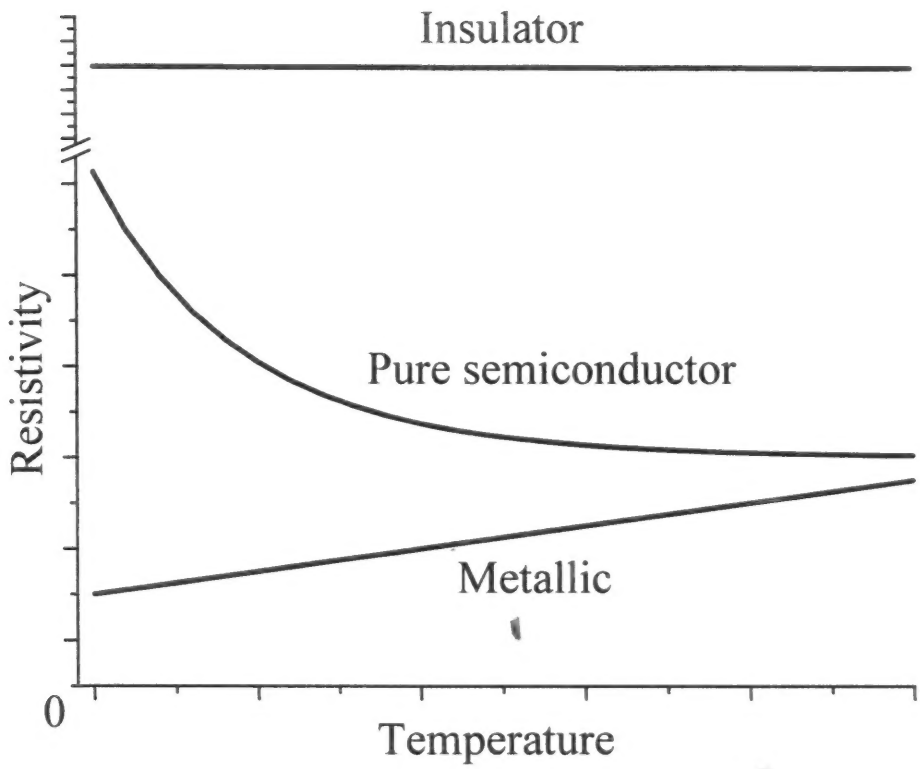

Figure 1–2. General relationship between resistivity and temperature for insulators, semiconductors and metals.

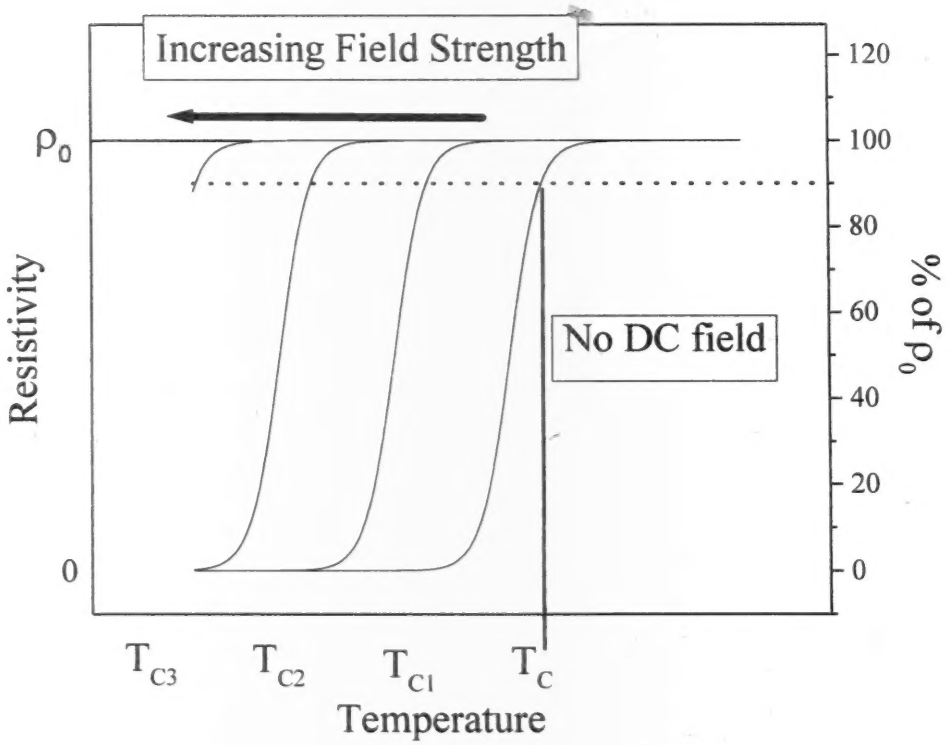

Figure 1–3. Hypothetical plot of resistivity vs temperature showing a superconducting transition from ρ_0, and the expected effect of an applied field. As the applied field is incrementally increased, the transition temperature is depressed. Here T_C is defined as the point where ρ falls to 90% of ρ_0.

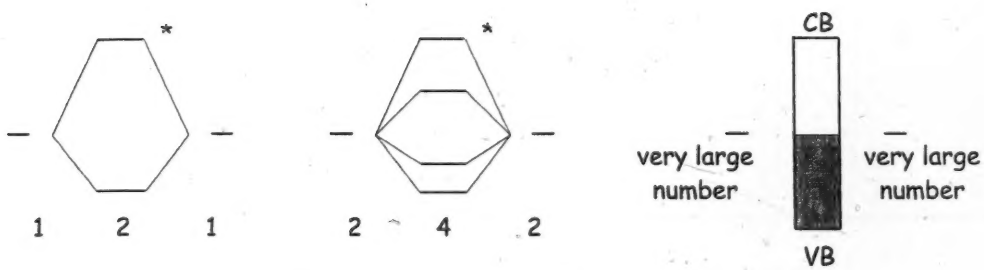

Figure 1–4. Origin of metallic band structure arising from atomic orbital overlap orbital interactions

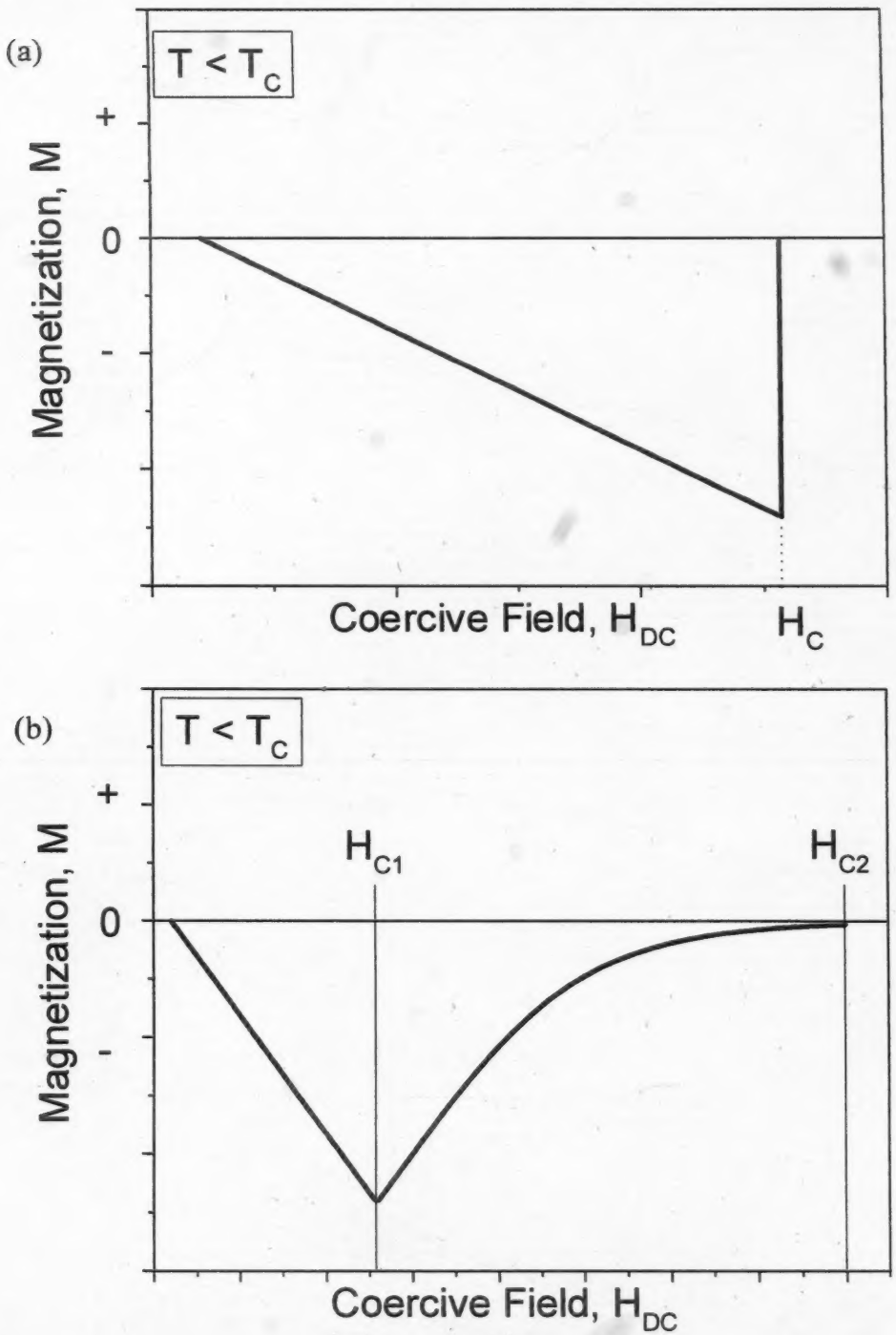

Figure 1–5. Hypothetical isothermal magnetisation versus coercive field of (a) a type I superconductor and (b) a type II superconductor.

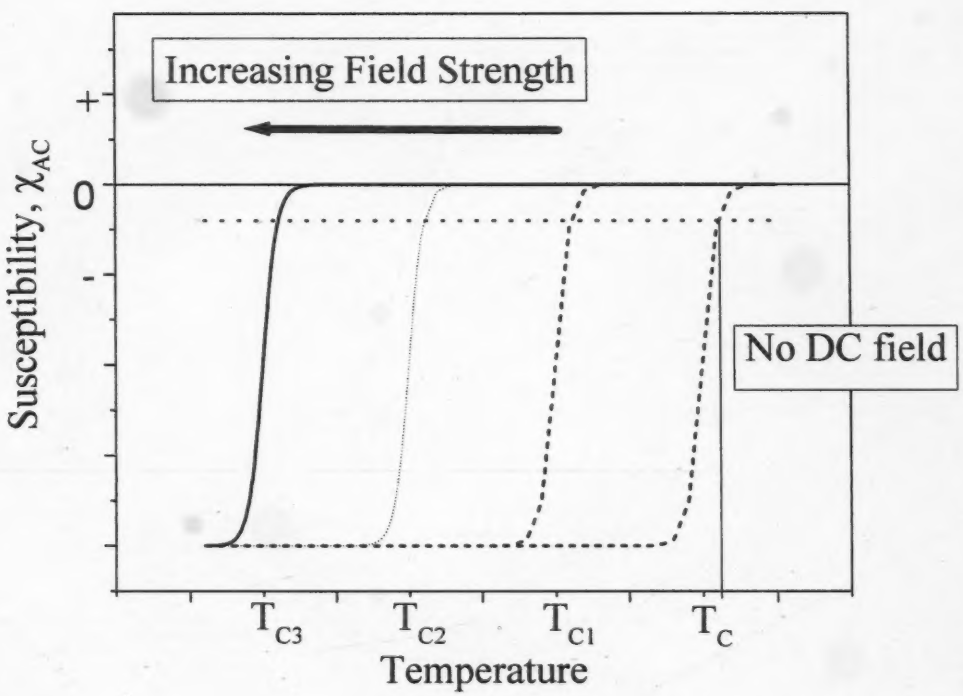

Figure 1–6. Hypothetical plot of ac susceptibility of a superconducting transition without an applied field and the expected effect of an applied field. As the applied field is increased the critical temperature is depressed. Here T_C is defined as 90% of the signal prior to the transition.

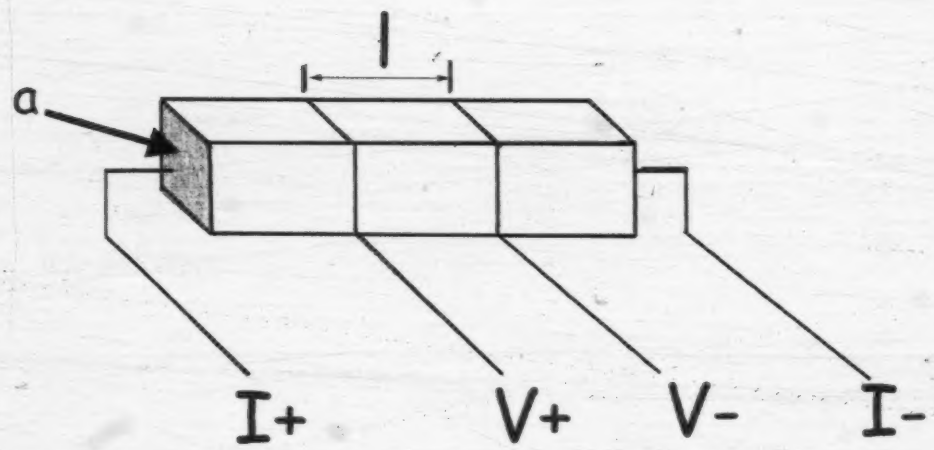

Figure 1–7. Layout of a four probe experiment used to determine resistivity.

References

(1) *Encyclopedia of materials Characterization: Surfaces, Interfaces, Thin Films* Brundle, C.R.; Evans, C.A. Jr.; Wilson, S.; Butterworth-Heinemann (publisher): Stoneham, 1992.

(2) *X-ray structure determination: A practical Guide Second Ed.*; Stout, G.H.; Jensen, L.H.; John Wiley & Sons Inc.: New York 1989.

(3) Sheldrick, G. M. *SHELXTL*, version 5.1; Bruker Analytical X-ray Systems, Inc.; Madison, WI, 1997.

(4) *Solid State Chemistry*; Smart, L.S.; Moore, E.; Second Ed., Stanley Thornes (publisher) Ltd.: Gloscher, 1998.

(5) *Properties of Materials*; White, M. -A.; Oxford University Press, New York, 1999.

(6) *Physics: For Scientists and Engineers*; Serway, R.A.; Third Ed., Saunders College Publishing: U.S.A., 1990.

(7) *Magnetochemistry*; Carlin, R.L.; Springer-Verlag: Berlin Heidelberg, 1986.

(8) *The Physical Principles of Magnetism*; Morrish, A.H.; John Wiley and Sons, Inc: New York, 1965.

(9) Kamerling-Onnes, H. *Akad. van Wetenschappen.* **1911**, *14*, 133, 818.

(10) Kim, S.-J.; Hu, S.; Uher, C.; Kanatzidis, M. G. *Chem. Mater.* **1999**, *11*, 3154.

(11) Chow, D.T.; McDonald, R.; Mar, A. *Inorg. Chem.* **1997**, *36*, 3750.

(12) Kim, H.; Klavins, P.; Kauzlarich, S.M. *Chem. Mater.* **2002**, *14*, 2308.

(13) Goodey, J.; Mao, J.; Guloy, A.M. *J. Am. Chem. Soc.* **2000**, *122*, 10478.

(14) Pecharsky, A.O.; Gschneidner Jr, K.A. *J. Alloys Compds*. **1999**, 67.

(15) Wang, Y.C.; Poduska, K.M.; Hoffmann, R.; DiSalvo, F.J. *J. Alloys Compds.* **2001**, *314*, 132.

(16) Kim, J.; Wang, C.; Hughbanks, T. *Inorg. Chem.* **1999**, *36*, 235.

(17) Papoian, G. A.; Hoffmann, R. *Angew. Chem. Int. Ed.* **2000**, *39*, 2408.

(18) Ferguson, M. J.; Hushagen, R. W.; Mar, A. *J. Alloys Compds.* **1997**, *249*, 191.

(19) Bolloré, G.; Ferguson, M. J.; Hushagen, R. W.; Mar, A. *Chem. Mater.* **1995**, *7*, 2229.

(20) Brylak, M.; Jeitschkoy, S. *Z. Naturforsch. B: Chem. Sci.* **1995**, *50*, 899.

(21) Raju, N. P.; Greendan J. E.; Ferguson, M. J.; Mar, A. *Chem. Mater.* **1998**, *10*, 3630.

(22) Ferguson, M. J. Ph. D. Thesis, University of Alberta, 2000.

(23) Salamakha, P.; Sologub, O.; Suemitsu, T.; Takabatake, T. *J. Alloys Compds.*, **2000**, *313*, L5.

(24) Haase, M.G.; Schmidt, T.; Richter, C.G.; Block, H.; Jeitschko, W. *J. S. S. Chem.* **2002**, *168*, 18.

(25) Zeng, L.; Franzen, H.F. *J Alloys Compds.* **2000**, *311*, 244.

(26) Moore, S.H.D.; Deakin, L.; Ferguson, M.J.; Mar, A. *Chem. Mater.* **2002**, *14*, 4867.

(27) Chan, J.Y.; Olmstead, M.M.; Kauzlarich, S.M. *Chem. Mater.* **1998**, *10*, 3583.

(28) Mozharivskyj, Y.; Franzen, H. F. *J. S. S. Chem.* **2000**, *152*, 478.

(29) Kaiser, J.W.; Jeitschko, W. *J. Alloys Compds.* **1999**, *291*, 66.

(30) Schimdt, T.; Jeitschko, W. *Z. Anorg. Allg. Chem.* **2002**, *628*, 927.

Chapter 2

Physical Properties and Bonding in RE_3TiSb_5 (*RE* = La, Ce, Pr, Nd, Sm)[†]

Introduction

The series of ternary rare-earth early-transition-metal antimonides RE_3MSb_5 (*RE* = La, Ce, Pr, Nd, Sm; *M* = Ti, Zr, Hf, Nb) has been reported, with the structures of La_3TiSb_5, La_3ZrSb_5, and La_3HfSb_5 determined from studying single crystals.[1,2] These compounds adopt a structure with a strongly one-dimensional character, consisting of isolated chains of face-sharing MSb_6 octahedra and linear skewers of Sb atoms that are separated by *RE* atoms (Figure 2–1). Compounds containing isolated face-sharing octahedral chains are well known in the chalcogenides and halides, and are frequently subject to electronic phase transitions associated with the inherent low-dimensionality of their structures.[3,4] In RE_3MSb_5, magnetic properties could be influenced by the presence of moments on both the rare-earth and transition metal, and electrical properties could be influenced by the degree of orbital overlap within and between chains. By systematically examining an isostructural family it is hoped that a relationship may be elucidated. Recent neutron diffraction studies on the isostructural ternary uranium compounds U_3TiGe_5 and U_3TiSn_5 revealed unusual magnetic behaviour involving ferromagnetic

---

[†] A version of this chapter has been published. Moore, S.H.D.; Deakin, L.; Ferguson, M.J.; Mar,A. *Chem. Mater.* **2002**, *14*, 4867. Copywright 2002 American Chemical Society

ordering along the chain axis and antiferromagnetic ordering perpendicular to it.[5] One family of the rare-earth compounds, RE_3TiSb_5, was chosen for the present investigation. Their magnetic and transport properties were measured, and single-crystal X-ray structures were determined for all members so that detailed band structure calculations could be carried out.

Experimental Section

Synthesis. Starting materials were elemental powders (La, Ce, Pr, Nd, Sm, 99.9%, Alfa-Aesar; Ti, 99.98%, Cerac; Sb, 99.998%, Aldrich; Sn, 99.8%, Cerac). Stoichiometric mixtures of the elements (total weight 0.250 g) in the presence of a Sn flux (0.5 g) were heated in evacuated fused-silica tubes (5-cm length; 10-mm i.d.) at 570 °C for 1 day and 950 °C for 2 days. While hot, the tubes were immediately centrifuged to remove the Sn flux. The remaining mass was treated with 6 M HCl to dissolve any remaining traces of Sn. Transport measurements were made on single crystals whose compositions were verified by EDX analyses on a Hitachi S-2700 scanning electron microscope. Magnetic measurements were made on ground samples whose purities were checked by X-ray powder diffraction on an Enraf-Nonius FR552 Guinier camera (Cu Kα radiation; Si standard). It is difficult to obtain completely pure products in the bulk, presumably because of problems in incongruent melting behaviour.

Structure Determination. The structure of La_3TiSb_5 has been determined previously from single-crystal X-ray diffraction data, but only cell parameters have been obtained for the remaining RE_3TiSb_5 members (RE = Ce, Pr, Nd, Sm).[1] In anticipation of a comparative study of their band structures, single-crystal diffraction data were collected. Intensity data were collected on a Bruker Platform / SMART 1000 CCD diffractometer at 22 °C using ω scans (0.2°). Crystal data are given in Table 2–1. Calculations were carried out with use of the SHELXTL (version 5.1) package.[6] Face-indexed numerical absorption corrections were applied. The centrosymmetric space group $P6_3/mcm$ was chosen and initial atomic positions were taken from the structure of La_3TiSb_5. Refinements proceeded in a straightforward manner, and revealed no evidence

for partial occupancy of sites. The difference electron density maps are featureless after the final refinements. Final values of the positional and displacement parameters are given in Table 2–2, interatomic distances are listed in Table 2–3, and further data in the form of a CIF are available as supporting information.

Transport Measurements. Standard four-probe techniques were applied on a Quantum Design PPMS system equipped with an ac transport controller (Model 7100). Electrical resistivities from 2 to 300 K were measured on needle-shaped single crystals, typically 0.05–0.10 mm wide and 0.5–0.8 mm long, that were previously screened by EDX analyses. A current of 0.10 mA oscillating at a frequency of 16 Hz was applied parallel to the needle axis (crystallographic *c* axis). Magnetoresistance data were obtained under zero-field-cooled conditions with the needle axis perpendicular to the applied field. All measurements were repeated at least twice on separate samples. Superconducting critical temperatures were determined at the point at which the resistivity drops to 90% of the normal value.

Magnetic Measurements. Magnetic data were obtained on ground samples placed in gelcap sample holders with a Quantum Design 9T–PPMS dc magnetometer / ac susceptometer between 2 and 300 K. A driving amplitude of 1 Oe and frequencies between 1000 and 5000 Hz were used in ac magnetic susceptibility measurements. In dc magnetic measurements, the susceptibility was corrected for contributions for the holder diamagnetism and the underlying sample diamagnetism using these values (emu f.u.$^{-1}$): *RE*, -20×10^{-6}; Ti, -15×10^{-6}; Sb, -15×10^{-6}. Complete magnetic characterization was plagued by difficulties in synthesis of phase-pure bulk samples. Samples were typically 70–90% pure, as gauged by X-ray powder diffraction. The major impurity is elemental

Sb, which is not superconducting under ambient pressures; in all cases, elemental Sn, which is superconducting at 3.722 K,[7] was not detectable.

Band Structure. One-electron tight-binding extended Hückel band structure calculations were performed on the $[TiSb_5]^{9-}$ substructure of RE_3TiSb_5 members, with use of the EHMACC suite of programs.[8,9] Extended Hückel parameters were taken from literature values and are listed in Table 2–4.[10] Properties were extracted from the band structure using 50 *k* points in the irreducible portion of the Brillouin zone.

Results and Discussion

Structure. Substitution of the rare-earth in RE_3TiSb_5 does not contract the structure uniformly. Examination of interatomic distances and angles reveals that maintaining a reasonable Ti–Sb(1) bond length within the face-sharing octahedral chains is most important. The Ti–Sb(1) distances remain relatively constant while the Ti–Ti and Sb(2)–Sb(2) contacts, parallel to the *c*-direction, gradually decrease upon substitution of a smaller *RE*. Consequently, the octahedral chains become increasingly distorted, flattening along the *c*-direction, as revealed by the deviation from ideal octahedral angles on going from La_3TiSb_5 (87.27(2)° and 92.73(2)°) to Sm_3TiSb_5 (86.62(2)° and 93.38(2)°). The shortest *RE*–*RE* contacts (~3.8 Å) occur along zigzag chains running parallel to the *c*-axis; the next closest distances are over ~4.8 Å. As discussed elsewhere, the Sb(2)–Sb(2) distances of ~3.1 Å within the linear skewers are suggestive of weak bonding interactions, modeled to a first approximation as one-electron bonds.[11] Applying the Zintl concept and assuming that full electron transfer takes place, the formulation $(La^{3+})_3(Ti^{4+})(Sb(1)^{3-})_3(Sb(2)^{2-})_2$ obtains. However, it is unclear whether the Ti–Ti distances, also of ~3.1 Å, indicate bonding, in which case the oxidation state assignment of Ti^{4+} would have to be modified. Nevertheless, the expectation based on inspection of the crystal structure is that the electronic properties will be highly anisotropic.

Transport Properties. Table 2–5 summarizes some of the electrical and magnetic properties of RE_3TiSb_5. Figure 2–2 shows the resistivity as a function of temperature for RE_3TiSb_5 members measured along the *c* axis. All compounds display metallic behaviour, with resistivities generally decreasing from room temperature down, but with prominent transitions occurring at low temperatures. In the high-temperature

regime (>50 K), La_3TiSb_5 shows a change in slope at 120 and 85 K. This feature occurs reproducibly in all samples of La_3TiSb_5 examined. In the other RE_3TiSb_5 members, the resistivity plots also show a curvature that becomes gradually less pronounced on proceeding to Sm_3TiSb_5. These transitions are reminiscent of behaviour observed in niobium and tantalum trichalcogenides,[3] but a definitive proposal for their origin is deferred until more detailed variable-temperature structural studies become available.

In the low-temperature regime (<50 K), some striking transitions are observed. La_3TiSb_5, Ce_3TiSb_5, and Nd_3TiSb_5 undergo show a drop to zero resistivity (within instrumental error) below T_C = 4.1, 4.0, and 3.7 K, respectively. Ce_3TiSb_5 also shows a local minimum in the resistivity curve at 25 K that is similar in behaviour observed in other Ce-containing Kondo systems.[12,13] Sm_3TiSb_5 displays an abrupt decrease in resistivity at 16 K, which is attributed to the occurrence of magnetic ordering of the Sm moments.

Magnetism and Magnetoresistance. All compounds show a positive magnetization at 2 K under applied fields greater than 500 Oe and no frequency dependence in the ac magnetic susceptibility from 1 to 5 kHz. For La_3TiSb_5 and Ce_3TiSb_5, the magnetic data are consistent with the single-crystal electrical resistivity data showing the occurrence of superconducting transitions, and are reported in detail herein.

In La_3TiSb_5, the transition to zero resistivity shifts to lower temperatures as a higher magnetic field is applied (Figure 2–3a). Evidence for superconductivity is further provided by the ac magnetic susceptibility measurements, which reveal both diamagnetic

shielding (under zero-field-cooled conditions) and the Meissner effect (under field-cooled conditions) (Figure 2–3b). The resistivity and magnetic susceptibility data establish T_C at

4.0 K. At 2 K, the dc magnetization curve (M vs H) reveals a profile characteristic of a type-II superconductor with critical fields of H_{C1} = 70 Oe and H_{C2} = 370 Oe (Figure 2–3c).

Although also a superconductor, Ce_3TiSb_5 is more complicated owing to the presence of a 4f electron in nominally Ce^{3+}. As in the La member, the resistivity shows a depression of T_C with greater applied magnetic fields (Figure 2–4a). The effective moment in Ce_3TiSb_5 at 300 K is 2.4 μ_B per Ce ion, close to that expected for Ce^{3+} (2.54 μ_B), and the θ_W value extracted from a fit of the dc magnetic susceptibility data at high temperature (not shown) to the Curie-Weiss law is –36 K. The negative χ'_{ac} values seen in the ac magnetic susceptibility data further support the occurrence of superconductivity with a T_C of 3.9 K (Figure 4b). At 2 K, the negative magnetization profile at very low fields (inset of Figure 2–4c) substantiates Ce_3TiSb_5 as a type-II superconductor with critical fields of H_{C1} = 75 Oe and H_{C2} = 150 Oe. Above 150 Oe, the magnetization becomes positive and displays two inflection points at 7600 and 16000 Oe (Figure 2–4c). Even under high-field conditions, up to H = 9 T, the magnetization has not reached saturation. These field-induced transitions observed below 3.9 K suggest the presence of co-existing superconducting and magnetically-ordered phases. At 2 K, the upper critical field of 150 Oe separates the superconducting from the magnetic regimes, but we have not determined the temperature dependence of this critical field. The nature of the magnetic phase remains an open question until further magnetic data on samples of greater purity or on large single crystals are available, preferably from neutron diffraction studies.

The magnetic data for Pr_3TiSb_5 and Nd_3TiSb_5 were deemed unreliable because not all impurities could be identified or significant amounts of other magnetic phases (such as $PrSb_2$) were observed. The resistivity of a single crystal of Nd_3TiSb_5 also shows a gradual decrease in T_C with greater applied fields similar to the behaviour seen in La_3TiSb_5 and Ce_3TiSb_5 (Figure 2–5). Although evidence from the magnetic data supporting a superconducting phase in Nd_3TiSb_5 is unavailable, the similar behaviour observed for the other members of this series lends credibility to the proposal that Nd_3TiSb_5 is also a superconductor below 3.7 K.

Although the Sm_3TiSb_5 sample was about 70% pure, the dc magnetic susceptibility vs temperature plot (Figure 2–6) reveals an anomaly at the same temperature (16 K) at which an abrupt transition occurs in the resistivity vs temperature plot (Figure 2–2e). The magnetic susceptibility does not obey the Curie-Weiss law and the isothermal magnetization at 2 K displays only positive values and a linear dependence with field (not shown). A possible interpretation is that the Sm 4f electrons are interacting with the conduction electrons to form a magnetic ground state that is favoured over a superconducting phase, and loss of spin-disorder scattering accounts for the abrupt decrease in resistivity below 16 K.

Band Structure. Calculations were carried out on the $[TiSb_5]^{9-}$ substructure of RE_3TiSb_5 compounds to confirm their metallic conductivity and to ascertain the extent of Ti–Ti and Sb–Sb bonding. Because it is a one-electron method, an extended Hückel calculation cannot account for the magnetic properties of these compounds, which arise primarily from the rare-earth ions that are neglected for consideration. In any case, reliable Hückel parameters for many rare-earth elements are unavailable. Although the

$[TiSb_5]^{9-}$ substructure can be considered as the superposition of independent chains of composition $[TiSb_3]^{5-}$ and $[Sb_2]^{4-}$, the rare-earth atoms can nevertheless be important if they participate in some degree of covalent bonding, effectively coupling these chains together.

The band dispersion for La_3TiSb_5 plotted along special symmetry lines within the Brillouin zone is shown in Figure 2–7. The most striking feature is that four disperse bands cross the Fermi level along ΓA, parallel to the axis of the $[TiSb_3]^{5-}$ and $[Sb_2]^{4-}$ chains, and that none of the bands cross the Fermi level along the other directions. The two widest bands along ΓA are associated with orbital interactions involving π-overlap of Ti d orbitals having a z-component with Sb(1) s-p hybrid orbitals within the $[TiSb_3]$ octahedral chains, as well as σ-overlap of Sb(2) p_z orbitals within the linear Sb skewers. The two narrower bands involve weak overlap of Ti d_{z2} orbitals mediated to a small extent by Sb(1) p_z orbitals. Along other directions, these bands show little or no dispersion, as expected given that the closest separation between $[TiSb_3]$ and $[Sb_2]$ chains is nearly 6 Å. Thus, La_3TiSb_5 can be regarded as a highly anisotropic metal with conduction along the needle axis being much greater than perpendicular to it.

The Fermi level falls in a region of very high density of states (DOS), as shown in Figure 2–8a, just below a large maximum in the curve. In this region, the states are dominated by contributions from Ti d orbitals. The occurrence of both narrow and wide bands near the Fermi level is often touted as a signature for superconductivity,[14,15] although this is not a sufficient condition; further analysis of the electron-phonon coupling processes is required.[16–18] In the case of RE_3TiSb_5, the position of the Fermi

level would be quite sensitive to minor changes arising from small contractions in the structure or involvement of the rare-earth atoms in covalent bonding.

Crystal orbital overlap population (COOP) curves are plotted in Figures 8b-d. The Ti–Sb bonding is optimized with all bonding states and no antibonding states occupied, resulting in an integrated overlap population of 0.505, typical of a strong single-bond interaction. For the longer 3.140 Å Sb–Sb and Ti–Ti contacts, some antibonding states are filled. The overlap population for the Sb–Sb contact is 0.227, roughly half of that expected for a single bond and consistent with the usual description of these distances in linear Sb chains as "one-electron" bonds. For the Ti–Ti contact, the overlap population is 0.078, which is small but emphatically positive, suggesting some degree of metal-metal bonding.

Assuming that the *RE* atoms play no role in mediating electronic conduction, similar band structure calculations on the $[TiSb_5]^{9-}$ substructure in the other members of the RE_3TiSb_5 series should reveal the effect of contracting the structure. Table 2–6 summarizes the results. Although the changes are small, the bands generally become more disperse and to maintain the same electron count, the Fermi level rises slightly. The Ti–Sb bonding remains of constant strength since the bond length has not changed significantly. However, there is a noticeable transfer of electron density from the Sb atoms to the Ti atoms, as seen in the trend in Mulliken charges. The bonding is already quite weak for the Sb–Sb and more so for the Ti–Ti contacts, but this electron transfer entails a minor strengthening of the Sb–Sb and minor weakening of the Ti–Ti bonds on going from La_3TiSb_5 to Sm_3TiSb_5.

The Ti d-bands are partially occupied, ranging from $d^{3.2}$ in La_3TiSb_5 to $d^{4.0}$ in Sm_3TiSb_5. However, there are narrow bands available very close to the Fermi level (Figure 2–8) and their relative positions would be sensitive to temperature, among other factors. This suggests that any of the RE_3TiSb_5 compounds are subject to electronic instability, and may account for the transitions in the electrical resistivity plots (Figure 2). Opposing the tendency for structural distortions that may ensue from these electronic transitions would be the impetus to maintain strong Ti–Sb bonds within the face-sharing octahedral chains.

Conclusion

The RE_3TiSb_5 compounds are metallic with the La, Ce, and probably Nd members being superconducting. The band structures of the $[TiSb_5]^{9-}$ substructures are similar in all compounds, suggesting that the occurrence of a superconductive phase is highly sensitive to the nature of the rare earth or the cell contraction. The magnetic data for powder samples of the La, Ce, and Sm members are consistent with the electrical resistivity data for single crystals; in particular, the critical temperatures determined from the two types of data are in agreement for the superconducting La and Ce members. In Ce_3TiSb_5, the observation of field-induced transitions suggests the occurrence of both superconducting and ordered magnetic phases below T_C. There is evidence for weak Ti–Ti bonding as one possible source for electronic instability. Examination of other RE_3MSb_5 (M = Zr, Hf, Nb) compounds, where M–M interactions are expected to be stronger, would therefore be of great interest.

Table 2–1. Crystallographic Data for RE_3TiSb_5 (RE = Ce, Pr, Nd, Sm). [a]

	Ce_3TiSb_5	Pr_3TiSb_5	Nd_3TiSb_5	Sm_3TiSb_5
fw	1077.01	1079.38	1089.37	1107.70
a (Å)	9.4277(4)	9.3835(2)	9.3517(3)	9.2758(3)
c (Å)	6.2316(3)	6.2156(2)	6.1976(2)	6.1581(2)
V (Å^3)	479.67(4)	473.96(2)	469.39(3)	458.86(3)
ρ_{calcd} (g cm^{-3})	7.457	7.563	7.708	8.017
μ (Mo Kα) (cm^{-1})	284.61	298.17	311.30	340.67
$R(F)$ for $F_o^2 > 2\sigma(F_o^2)$ [b]	0.039	0.020	0.023	0.042
$R_w(F_o^2)$ [c]	0.077	0.042	0.057	0.075

[a] For all structures listed, space group is D_{6h}^3–$P6_3/mcm$ (No. 193), $Z = 2$, $T = 22$ °C, and $\lambda = 0.71073$ Å. [b] $R(F) = \sum \| F_o | - | F_c \| / \sum | F_o |$. [c]

$$R_w(F_o^2) = \left[\sum \left[w(F_o^2 - F_c^2)^2 \right] / \sum w F_o^4 \right]^{1/2}; \; w^{-1} = \left[\sigma^2(F_o^2) + (ap)^2 + (bp) \right] \text{ where}$$

$$p = \left[\max(F_o^2, 0) + 2F_c^2 \right] / 3.$$

Table 2–2. Positional and Equivalent Isotropic Displacement Parameters for RE_3TiSb_5 (RE = Ce, Pr, Nd, Sm).

	Ce_3TiSb_5	Pr_3TiSb_5	Nd_3TiSb_5	Sm_3TiSb_5
RE at 6*g* (*x*, 0, 1/4)				
x	0.61740(8)	0.61738(5)	0.61757(5)	0.61727(9)
U_{eq} (Å^2) [a]	0.0081(2)	0.0097(1)	0.0104(2)	0.0089(2)
Ti at 2*b* (0, 0, 0)				
U_{eq} (Å^2) [a]	0.0081(8)	0.0094(4)	0.0102(5)	0.0079(8)
Sb(1) at 6*g* (*x*, 0, 1/4)	0.25307(10)	0.25426(6)	0.25545(7)	0.25715(11)
x	0.0078(2)	0.0092(1)	0.0099(2)	0.0082(2)
U_{eq} (Å^2) [a]				
Sb(2) at 4*d* (1/3, 2/3, 0)	0.0080(3)	0.0096(2)	0.0103(2)	0.0082(3)
U_{eq} (Å^2) [a]				

[a] U_{eq} is defined as one-third of the trace of the orthogonalized U_{ij} tensor.

Table 2–3. Selected Interatomic Distances (Å) in RE_3TiSb_5 (*RE* = La, Ce, Pr, Nd, Sm).

	La_3TiSb_5 [a]	Ce_3TiSb_5	Pr_3TiSb_5	Nd_3TiSb_5	Sm_3TiSb_5
RE–Sb(1) (×2)	3.2064(8)	3.1776(6)	3.1649(4)	3.1549(4)	3.1345(6)
RE–Sb(2) (×4)	3.3598(4)	3.3255(3)	3.3114(2)	3.3011(2)	3.2747(3)
RE–Sb(1) (×2)	3.3815(8)	3.3466(5)	3.3330(3)	3.3185(3)	3.2920(5)
RE–Sb(1)	3.496(1)	3.4348(12)	3.4074(7)	3.3865(8)	3.3403(13)
RE–*RE* (×2)	3.858(1)	3.8221(9)	3.8094(5)	3.7997(6)	3.7700(9)
Ti–Sb(1) (×6)	2.859(1)	2.8495(8)	2.8472(5)	2.8473(6)	2.8390(9)
Ti–Ti (×2)	3.1400(5)	3.1158(2)	3.1078(1)	3.0988(1)	3.0790(1)
Sb(2)–Sb(2) (×2)	3.1400(5)	3.1158(2)	3.1078(1)	3.0988(1)	3.0790(1)

[a] At –60 °C.[1]

Table 2–4. Extended Hückel Parameters.

atom	orbital	H_{ii} (eV)	ζ_{i1}	c_1	ζ_{i2}	c_2
Ti	4s	–8.48	1.50			
	4p	–4.60	1.50			
	3d	–9.26	4.55	0.4391	1.60	0.7397
Sb	5s	–18.8	2.323			
	5p	–11.7	1.999			

Table 2–5. Summary of Resistivity and Magnetism Data for RE_3TiSb_5.

	La_3TiSb_5	Ce_3TiSb_5	Pr_3TiSb_5	Nd_3TiSb_5	Sm_3TiSb_5
$\rho_{300\ K}$ (Ω cm)	2.0×10^{-3}	1.3×10^{-4}	1.5×10^{-4}	1.5×10^{-4}	2.8×10^{-4}
$\rho_{300\ K}/\rho_{5\ K}$	5.0	2.3	12	8.2	6.1
T_C (K)	4.1[a] / 4.0[b]	4.0[a] / 3.9[b]		3.7[a]	
H_{C1}, H_{C2} (2 K) (Oe)	70, 370	70, 150			

[a] Determined from ρ vs T plot. [b] Determined from χ'_{ac} vs T plot.

Table 2–6. Mulliken charges and integrated overlap populations for $[TiSb_5]^{9-}$ substructure in RE_3TiSb_5.

	La_3TiSb_5	Ce_3TiSb_5	Pr_3TiSb_5	Nd_3TiSb_5	Sm_3TiSb_5
ε_f (eV)	–8.71	–8.65	–8.64	–8.62	–8.59
Mulliken charge					
Ti	–0.39	–0.65	–0.80	–0.87	–1.18
Sb	–1.72	–1.68	–1.64	–1.61	–1.56
Overlap					
population	0.505	0.506	0.506	0.505	0.506
Ti–Sb	0.227	0.229	0.220	0.231	0.232
Sb–Sb	0.078	0.077	0.074	0.077	0.067
Ti–Ti					

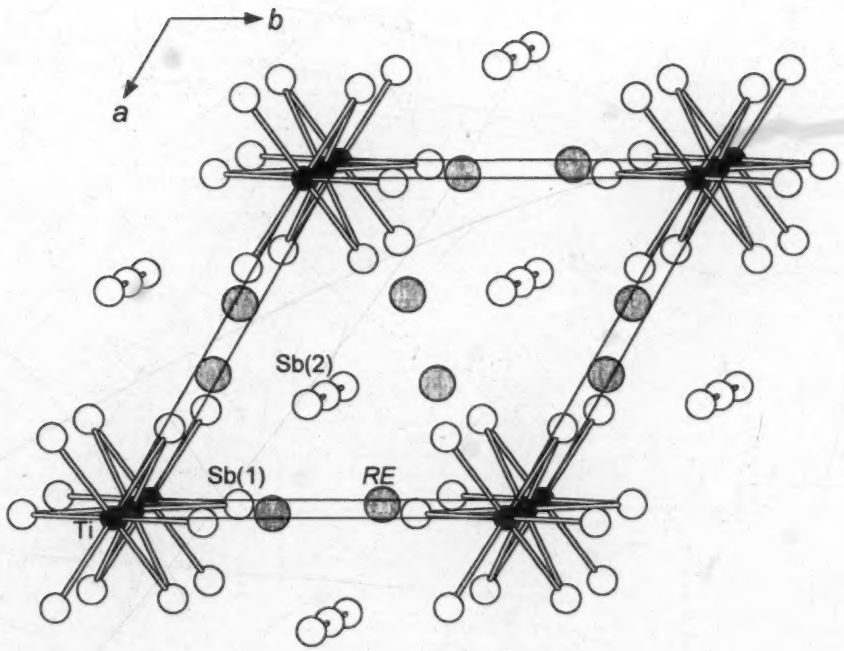

Figure 2–1. Structure of RE_3TiSb_5 (*RE* = La, Ce, Pr, Nd, Sm) viewed down the *c* axis. The large lightly shaded circles are *RE* atoms, the small solid circles are Ti atoms, and the medium open circles are Sb atoms.

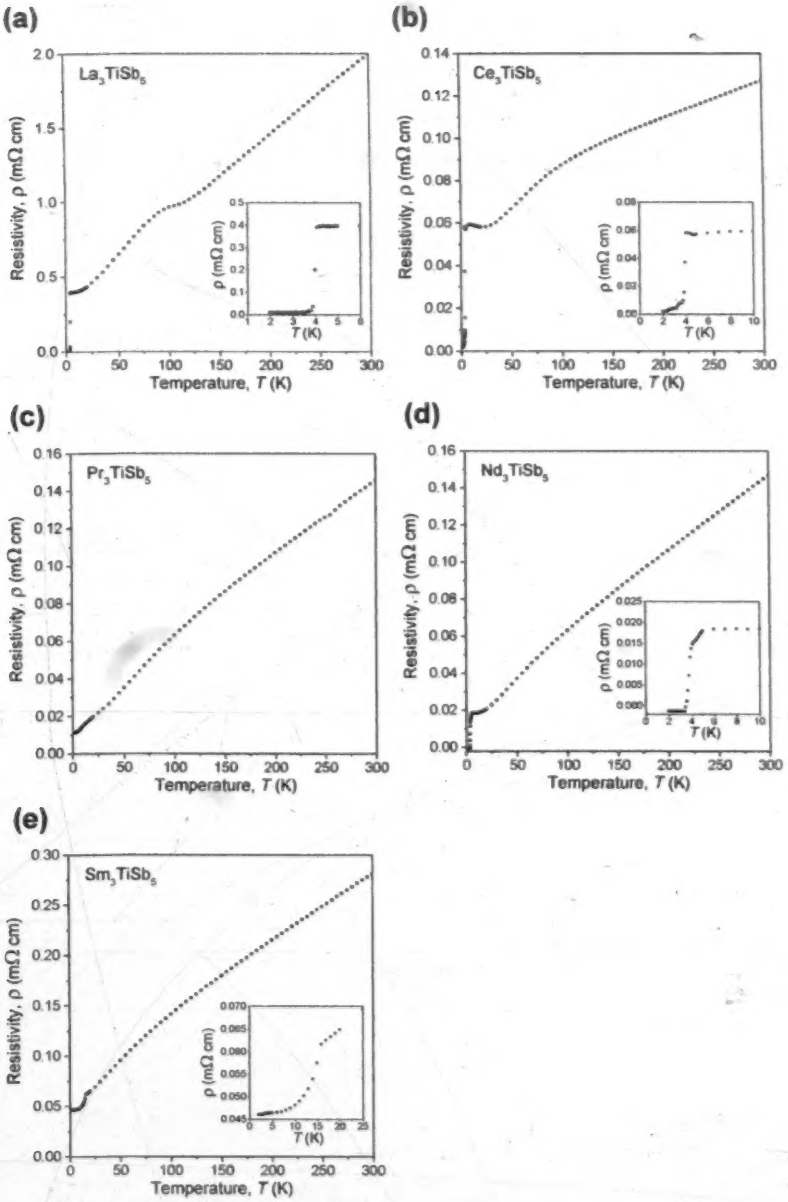

Figure 2–2. Zero-field electrical resistivity of single crystals of RE_3TiSb_5 (RE = (a) La, (b) Ce, (c) Pr, (d) Nd, (e) Sm) measured along the c axis between 2 and 300 K. Insets show low-temperature behaviour.

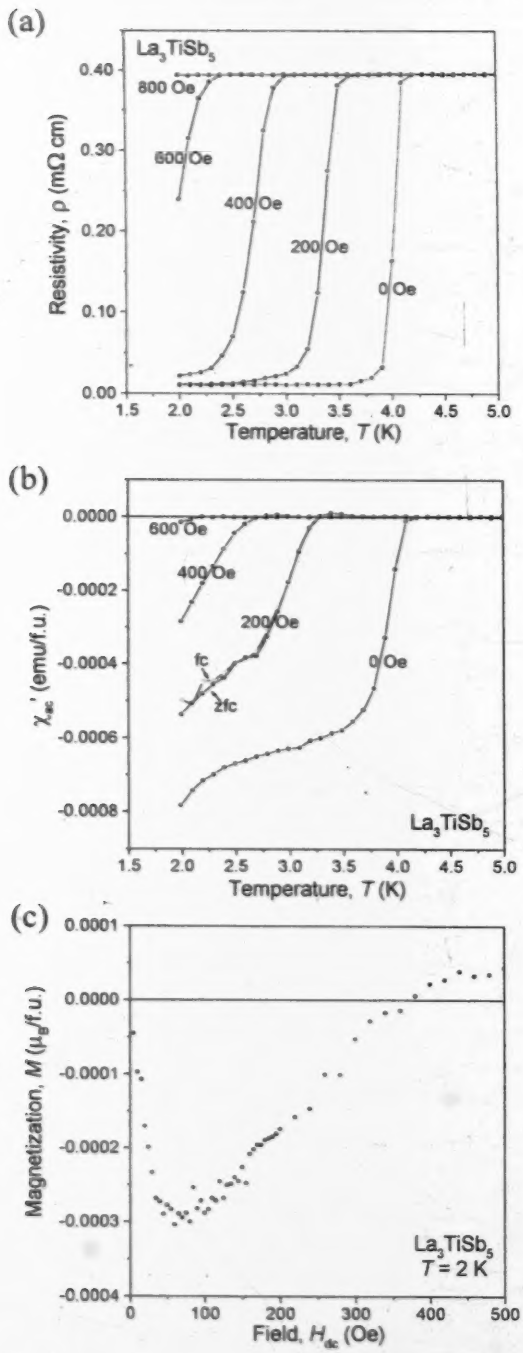

Figure 2–3. (a) Field dependent single-crystal electrical resistivity, (b) temperature dependence of zero-field-cooled ac magnetic susceptibility under various applied fields (and an additional field-cooled run at 200 Oe), and (c) isothermal magnetization at 2 K for La_3TiSb_5. Lines shown are included only to guide the eye.

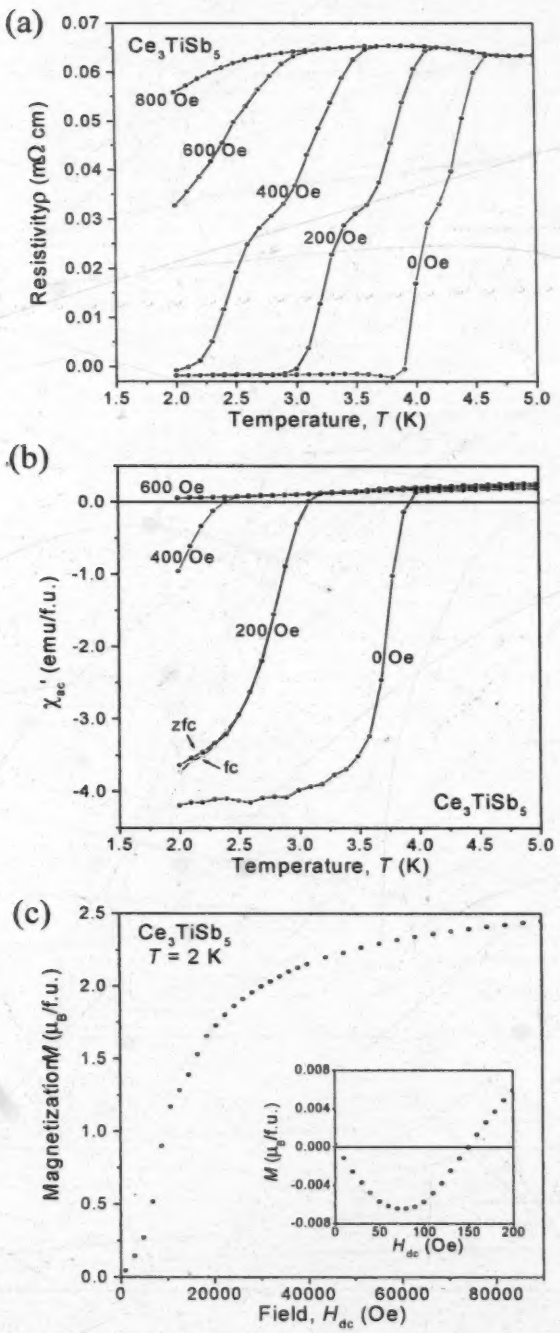

Figure 2–4. (a) Field dependent single-crystal electrical resistivity, (b) temperature dependence of zero-field-cooled ac magnetic susceptibility under various applied fields (and an additional field-cooled run at 200 Oe), and (c) isothermal magnetization at 2 K for Ce_3TiSb_5. Lines shown are included only to guide the eye.

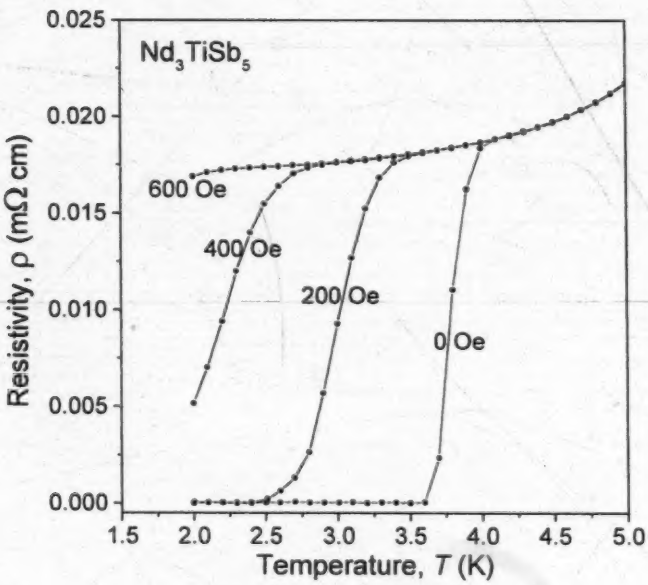

Figure 2–5. Field dependent single-crystal electrical resistivity for Nd_3TiSb_5

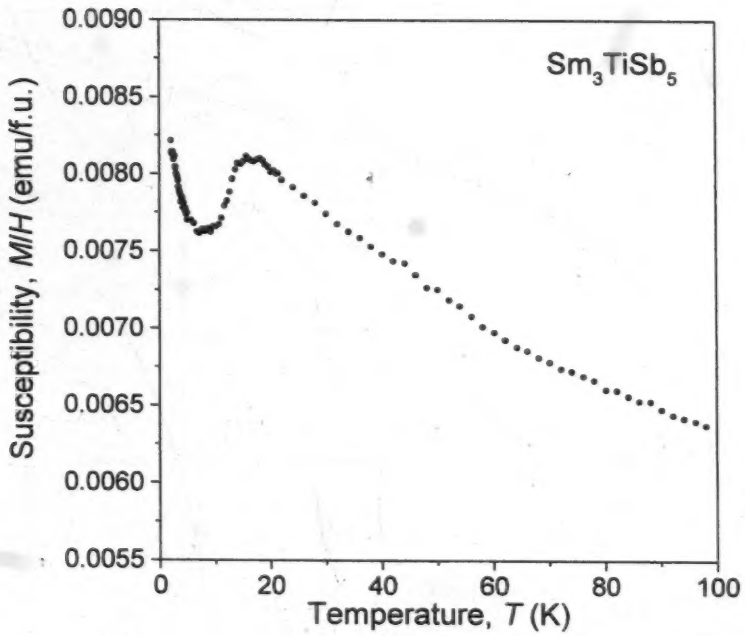

Figure 2–6. Magnetic susceptibility (M/H) of Sm_3TiSb_5 under an applied field of 1.0 T

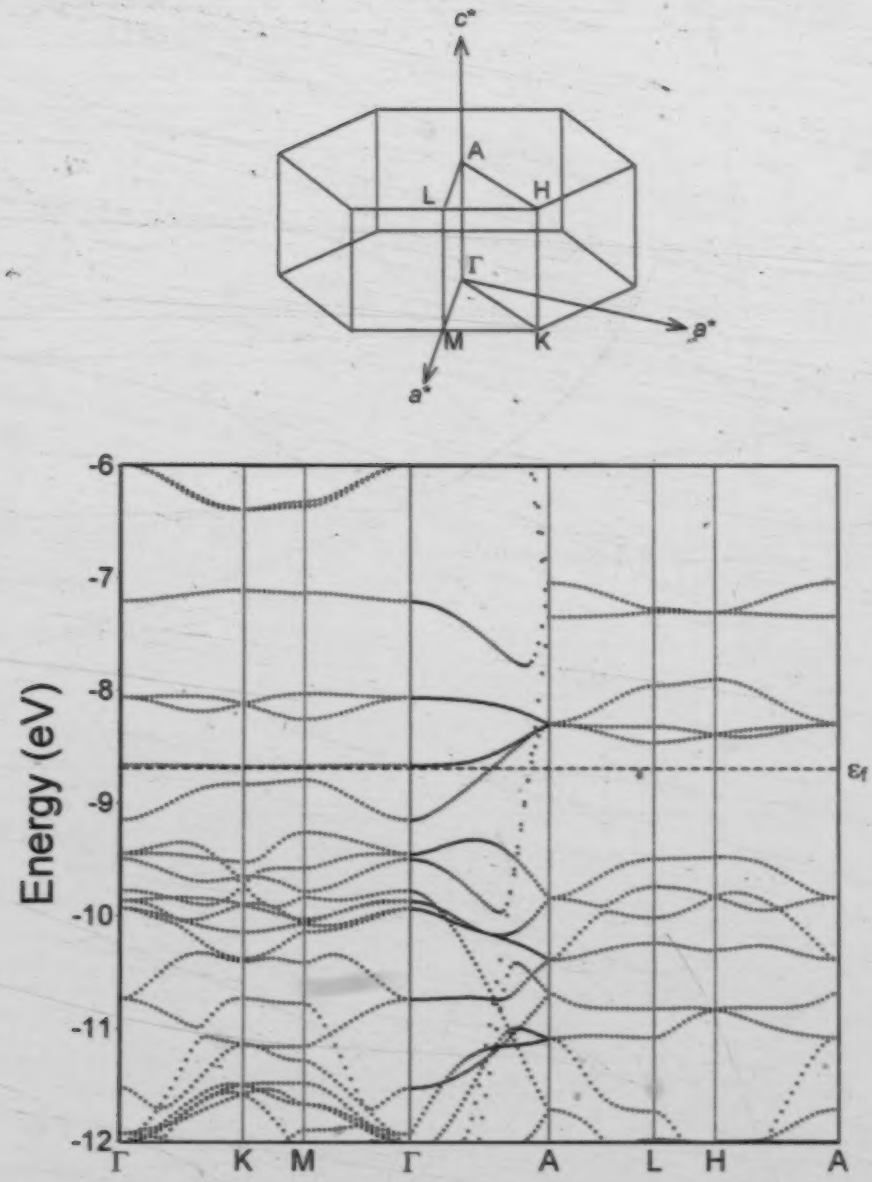

Figure 2–7. Band dispersion curves along special symmetry lines for the $[TiSb_5]^{9-}$ substructure in La_3TiSb_5. The dashed horizontal line marks the Fermi level ($\varepsilon_f = -8.71$ eV). A representation of the hexagonal Brillouin zone is shown with the irreducible wedge outlined.

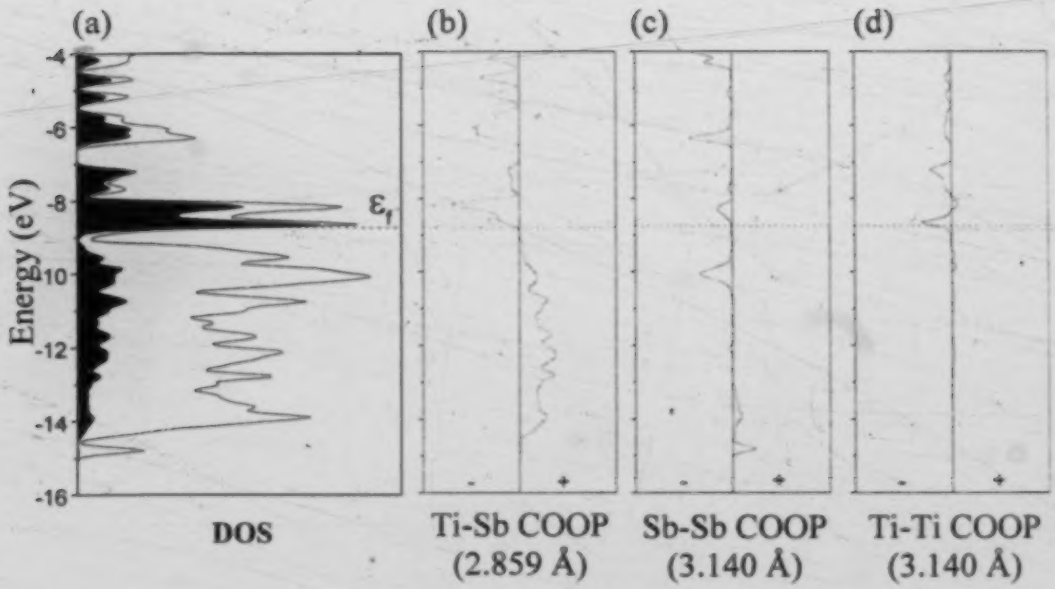

Figure 2–8. (a) Density of states (DOS) (with the Ti projection shown by the filled area; what remains of the DOS is the Sb projection) and crystal orbital overlap population (COOP) curves for the (b) Ti–Sb, (c) Sb–Sb, and (d) Ti–Ti contacts in the $[TiSb_5]^{9-}$ substructure in La_3TiSb_5. The dashed horizontal line marks the Fermi level ($\varepsilon_f = -8.71$ eV).

References

(1) Bolloré, G.; Ferguson, M.J.; Hushagen, R.W.; Mar, A. *Chem. Mater.* **1995**, *7*, 2229.

(2) Ferguson, M.J.; Hushagen, R.W.; Mar, A. *J. Alloys Compd.* **1997**, *249*, 191.

(3) *Theoretical Aspects of Band Structures and Electronic Properties of Pseudo-One-Dimensional Solids*; Kanimura, H., Ed.; Physics and Chemistry of Materials with Low-Dimensional Structures, Series B; D. Reidel: Dordrecht, The Netherlands, 1985.

(4) Whangbo, M.-H., Foshee, M.J.; Hoffmann, R. *Inorg. Chem.* **1980**, *19*, 1723.

(5) Boulet, P.; Gross, G.M.; André, G.; Bourée, F.; Noël, H. *J. Solid State Chem.* **1999**, *144*, 311.

(6) Sheldrick, G.M. *SHELXTL*, version 5.1; Bruker Analytical X-ray Systems, Inc.; Madison, WI, 1997.

(7) Roberts, B.W. *Properties of Selected Superconductive Materials*; US Government Printing Office: Washington, DC, 1978.

(8) Whangbo, M.-H.; Hoffmann, R. *J. Am. Chem. Soc.* **1978**, *100*, 6093.

(9) Hoffmann, R. *Solids and Surfaces: A Chemist's View of Bonding in Extended Structures*; VCH Publishers: New York, 1988.

(10) Kleinke, H. *J. Am. Chem. Soc.* **2000**, *122*, 853.

(11) Papoian, G.A.; Hoffmann, R. *Angew. Chem. Int. Ed.* **2000**, *39*, 2408.

(12) Chevalier, B.; Etourneau, J. *J. Mater. Chem.* **1999**, *9*, 1789.

(13) Gordon, R.A.; DiSalvo, F.J.; Pöttgen, R. *J. Alloys Compd.* **1995**, *228*, 16.

(14) Felser, C. *J. Solid State Chem.* **2001**, *160*, 93.

(15) Simon, A. *Angew. Chem. Int. Ed. Engl.* **1997**, *36*, 1788.

(16) Deng, S.; Simon, A.; Köhler, J. *Angew. Chem. Int. Ed.* **1998**, *37*, 640.

(17) Deng, S.; Simon, A.; Köhler, J. *Solid State Sci.* **2000**, *2*, 31.

(18) Deng, S.; Simon, A.; Köhler, J. *J. Phys. Chem. Solids* **2001**, *62*, 1441.

Chapter 3

Tin Doped Rare-Earth Titanium Antimonides $RETi_3(Sn_{0.1}Sb_{0.9})_4$ (*RE* = Nd, Sm) with a Layered Structure

Introduction

The conventional definition of a layered material is one in which covalently bonded layers are held together by weak van der Waals forces. Guest atoms can be reversibly intercalated between the layers, as in Li-intercalated graphite. A modified definition places emphasis on the degree of anisotropy, which may arise from the arrangement of atoms instead of the nature of the bonding. In this way, some intermetallic compounds may be regarded as being layered.

The structures of many rare earth transition metal antimonides have some degree of low dimensionality. Some have layers composed exclusively of heteroatomic polyhedra, such as $CeNi_2Sb_2$ ($CaBe_2Ge_2$ type),[1] whereas others possess additional homoatomic layers such as Sb square sheets in $RECrSb_3$ (*RE* = La, Ce).[2,3] The layered nature of these phases creates potential for anisotropic magnetic and transport behaviour, as in $SmCrSb_3$,[4] where the temperature dependence of the resistivity is metallic parallel to the layers but undergoes a dramatic change in slope at the Curie temperature perpendicular to the layers. The inclusion of both rare-earth and transition metals can lead to cooperative magnetic effects arising from both centres as in $NdCrSb_3$.[5]

The compounds RE_3MSb_5 (RE = La, Ce, Pr, Nd, Sm, Gd; M = Ti, Zr, Hf, Nb) phases have been prepared by heating stoichiometric mixtures of the elements in a tube furnace using a Sn flux.[6] The crystalline products are part of a mixture of SnSb, RE_xSb_y or M_xSb_y powders. The conditions leading to high product yield and good quality crystal growth may sometimes differ.

Examination of Sn flux relations having distinctly different heating programs targeting the synthesis of RE_3TiSb_5 suggested the existence of a new phase. Initial evidence from EDX analysis showed a different atomic composition than expected for the RE_3TiSb_5 phase. Samples of this new phase contained Sn in the same proportion; from experience, it is known that the RE_3TiSb_5 phase does not incorporate Sn into its structure. The phase was then structurally characterized by single crystal X-ray diffraction methods, revealing a new layered structure. Efforts were made to synthesize sufficiently large samples for further study. This chapter presents the structure of a new Sn-doped $RETi_3Sb_4$ (RE = Nd, Sm) phase, as well as synthetic efforts to prepare the phase rationally and to extend the family to include other rare earths.

Experimental Section

Synthesis. Starting materials were elemental powders (La, Ce, Pr, Nd, Sm, 99.9%, Alfa-Aesar; Ti, 99.98%, Cerac; Sb, 99.998%, Aldrich; Sn, 99.8%, Cerac). Mixtures of the elements (total weight 0.250 g) in the presence of a Sn or Sb flux were sealed in evacuated fused-silica tubes (5-cm length; 10-mm i.d.) and heated under the conditions shown in Table 3–1. While hot, the tubes were immediately centrifuged to remove the bulk of the flux. For Sn flux reactions, the remaining mass was treated with 6 M HCl to dissolve any traces of Sn. Arc melting reactions were also carried out with a 5% excess of Sb or Sn added to compensate for loss due to volatility of the element. The mixtures were cold pressed into pellets, weighed, and arc melted under a titanium gettered argon atmosphere. Cooled pellets were flipped and re-melted twice more before being weighed; typical mass loss was 5%. Single crystal compositions were verified by EDX analyses on a Hitachi S-2700 scanning electron microscope. Sample purity was confirmed by X-ray powder diffraction on an Enraf-Nonius FR552 Guinier camera (Cu Kα radiation; Si standard).

Single crystals of the $RETi_3(Sn_{0.1}Sb_{0.9})_4$ phase used for X-ray diffraction characterization were isolated from RE_3TiSb_5 (*RE* = Nd, Sm) reactions prepared from a Sn flux. The $NdTi_3(Sn_{0.1}Sb_{0.9})_4$ crystal was isolated from a reaction heated at 570 °C for one day and 950 °C for two days, cooled to 20 °C, and then heated to 950 °C before being centrifuged. The $SmTi_3(Sn_{0.1}Sb_{0.9})_4$ crystal was isolated from a reaction heated at 700 °C for two days, and then centrifuged. These reactions were repeated but did not yield any other crystals.

To determine whether a $RETi_3Sb_4$ (*RE* = Nd, Sm) phase always coexists with the

RE_3TiSb_5 phase, products from previous reactions to prepare RE_3TiSb_5 were evaluated by X-ray powder diffraction. The new phase was detected in various reactions at a level near the detection limit for XRD techniques (~5%). To investigate the degree of RE substitution, theoretical X-ray diffraction patterns were prepared and matched against observed patterns of the products of RE_3TiSb_5 (*RE* = La, Ce, Pr, Nd, Sm) reactions. Except for minor shifts in some lines in the diffraction patterns, the good agreement between theoretical and observed patterns indicates that the phases were present in the reactions. Reactions to prepare these phases rationally, reliably, and in larger yields were then carried out.

EDX analysis of the $RETi_3(Sn_{0.1}Sb_{0.9})_4$ (*RE* = Nd, Sm) samples showed the presence of all indicated elements and a Sn:Sb ratio of 1:9. To examine the extent of possible Sn–Sb substitution, a variable composition study was conducted. Because the single crystals of $RETi_3(Sn_{0.1}Sb_{0.9})_4$ were first isolated from RE_3TiSb_5 (*RE* = Nd, Sm) reactions, attention was focused on these rare earths in anticipation that they were most amenable to form crystals. Arc melting reactions were carried out for $SmTi_3(Sn_xSb_{1-x})_4$ where $x = 0, 0.2, 0.4, 0.6, 0.8, 1.0$.

Structure determination. Initial cell parameters were determined by Weissenberg photography. Final cell parameters were refined by least squares fitting of 4164 and 3297 reflections for the Nd and Sm phases, respectively. Intensity data collection was carried out on a Bruker Platform / SMART 1000 CCD diffractometer at 22 °C using ω scans (0.2 °). Crystal data are given in Table 3–2. All calculations were carried out with the SHELXTL (version 5.1) package.[7] A face-indexed Gaussian-type absorption correction was applied. Systematic absences suggested an *F*-centred unit cell

and the possible space groups *Fmmm*, *Fmm*2, and *F*222. The centrosymmetric space group *Fmmm* was chosen over the non-centrosymmetric and chiral space groups. The positions of all atoms were located by direct methods. Subsequent refinements showed all sites to be fully occupied and the displacement parameters to be well behaved. In the final refinement, the difference map was featureless: $\Delta\rho_{min}$, $\Delta\rho_{max}$ = –3.01, 1.37 e Å^{-3} for the Nd phase and $\Delta\rho_{min}$, $\Delta\rho_{max}$ = –2.44, 2.32 e Å^{-3} for the Sm phase. Because Sn and Sb cannot be distinguished on the basis of their similar scattering factors, their occupancies were fixed to reflect the ratio found from EDX analysis. For the same reason, it could not be shown if Sn preferentially occupies any of the three Sb sites or if it was equally distributed among all three; final refinement proceeded under the latter assumption. Final positional and equivalent isotropic displacement parameters are presented in Table 3–3 and selected bond lengths are listed in Table 3–4. The unit cell is depicted in Figure 3–1.

The faintness of the XRD patterns for the target phases in the exploratory reactions implied low yields. Moreover, the theoretical diffraction patterns typically had fewer than 17 reflections with relative intensities greater then 10%. The uncertainties in the unit cell parameters are thus larger than typical. The results are shown in Table 3–5; refinement summaries are listed in the appendix.

Discussion

Synthesis. Attempts to prepare $RETi_3Sb_4$ rationally always resulted in RE_3TiSb_5 as the major product. Figure 3–2 shows a plot of the unit cell volume vs *RE*. The variable composition study showed that the $SmTi_3(Sn_xSb_{1-x})_4$ phase was only detectable at very low concentrations ($0 \leq x \leq 0.2$) of Sn, suggesting a narrow composition range. Furthermore the phase could be made free of Sn in an arc melted reaction, but not free of Sb. The variable temperature study indicated that the $SmTi_3Sb_4$ phase is favoured at temperatures higher than 700 °C along with Ti_2Sb. In order for $SmTi_3Sb_4$ phase to be formed, the samples must be heated to at least 700 °C; even then the compound will not dominate the reaction products. After examining all the reaction conditions for those reactions whose powder diffraction pattern showed the $RETi_3Sb_4$ phase, there were few common synthetic aspects. It is believed that another aspect of the synthetic methodology, such as temperature gradients, is not being controlled in the tube furnace reactions yielding inconsistent results.

Structure. For the purposes of the following discussion the disordered Sn/Sb sites are referred to as "*X*". The structure of $RETi_3(Sn_{0.1}Sb_{0.9})_4$ consists of layers of face sharing $TiX_{4/6}X_{2/3}$ octahedra stacked perpendicular to [001]. The basic coordination polyhedron is a distorted $TiX_{4/6}X_{2/3}$ octahedron, of which there are two types. Type one is shown in Figure 3–3(a), and is oriented such that its *X*(2)–Ti(2)–*X*(2) axis is parallel with [100]. The *X*(2) atoms are both displaced resulting in a *X*(2)–Ti(2)–*X*(2) bond angle of 155.12(5)° and 155.46(6) ° for the Nd and Sm phases, respectively, a significant deviation from the ideal value of 180°. The *X*(1)–*X*(1) distance is slightly shorter than the *X*(3)–*X*(3) distance. The Ti(2)–*X* distances in $RETi_3(Sn_{0.1}Sb_{0.9})_4$ are comparable to the Ti–Sb

distances in other compounds (Table 3–6). The type two octahedron, Ti(1)$X_{4/6}X_{2/3}$, shown in Figure 3–3(b), shows similar interatomic distances and angles; in contrast, the X(1) and X(3) centres are not coplanar.

Six of the distorted octahedra (two type one and four type two) share faces to create a unit with pseudohexagonal symmetry as shown in Figure 3–4. The motif continues as more octahedra add to the sheet's edge in a face sharing fashion extending it along the *ab* plane. Each X(3)–X(3) edge is shared by another Ti$X_{4/6}X_{2/3}$ octahedron doubling the sheet's thickness along [001]. The second sheet of octahedra is arranged in mirror fashion to the first sheet above to create a full layer. This doubling creates a cavity between the two sheets, which is hexagonal bipyramidal in shape measuring 3.1855(10) Å and 3.2020(11) Å along its principal axis, for the Nd and Sm phases respectively. Although these are within the interlayer distance of elemental antimony (3.36 Å),[8] they are significantly longer than Sb–Sb single bond (2.91 Å)[8] implying that Sb–Sb interactions are present but weak. It is interesting that this distance is larger for the Sm structure than for the Nd structure, whereas the opposite is true for all other interatomic distances in Table 3–5.

The *RE* atom is situated in the pseudohexagonal depression created by six Ti$X_{4/6}X_{2/3}$ octahedra. It interacts with two X atoms from the adjacent layer, giving a CN of 9. All *RE*–X distances are comparable to those in RE_3TiSb_5 (*RE* = Nd, Sm).

*RE*Ti$_3$(Sn$_{0.1}$Sb$_{0.9}$) can be compared with known layered ternary transition metal antimonides. We considered the REM_2Sb_2 ($CaBe_2Ge_2$–type),[9] REM_2Sb_2 ($ThCr_2Si_2$–type),[10] $REMSb_2$ ($ZrCuSi_2$–type)[11] and *RE*$CrSb_3$ structures.[2,3] In general, as the phases become more Sb-rich, homoatomic structural features in the form of square nets appear.

These structures possess layers of either edge-sharing tetrahedra or face-sharing octahedra and the CN of the rare earth atom is 9 or 10. All of these structure types are closely related. The $CaBe_2Ge_2$–type structure contains alternating layers of $M Sb_{4/4}$ and $Sb M_{4/4}$ edge-sharing tetrahedra. The *RE* atoms lie between these layers, with a bicapped square antiprism coordination geometry. The $ThCr_2Si_2$–type structure is related to the $CaBe_2Ge_2$–type structure in that each layer is $M Sb_{4/4}$. The *RE* atoms lie on a mirror plane between the two layers and have bicapped square prism coordination geometry. The $ZrCuSi_2$–type structure differs from this last with introduction of an Sb square net, situated on the mirror plane between the two layers. The *RE* atoms are positioned between a $M Sb_{4/4}$ tetrahedral layer and an Sb square sheet. The coordination geometry of the *RE* atom is now a monocapped square antiprism. In the $RECrSb_3$ structure, the layers consist of chains of face-sharing octahedra. Figure 3–6 compares the $RECrSb_3$ and $RETi_3(Sn_{0.1}Sb_{0.9})_4$ structures. The $RETi_3(Sn_{0.1}Sb_{0.9})_4$ phase is not Sb-rich and does not contain a homoatomic Sb layer, as expected. The *RE* has a reasonable CN of 9, but its coordination geometry is atypical. Futher, the layers are twice as thick compared to the other structures. This suggests that it may be worthwhile targeting structures containing increasingly thicker layers.

Applying the Zintl concept to $RETi_3Sb_4$ and assuming the presence of RE^{3+} ions, the anionic network $[Ti_3Sb_4]^{3-}$ is obtained. If Ti is assumed to be +4, an unrealistic charge of –3.75 is obtained for Sb. The absence of any short *X*–*X* distances suggests the presence of isolated Sb^{3-} atoms. This new assumption yields Ti^{3+}, which could participate in metal-metal bonding by virtue of its d^1 electron count The Ti–Ti distances are within that of the sum of metallic radii of 2.92 Å,[12] indicating the possibility of metal-

metal bonding.

The Ti(1) centres are arranged in linear chains that run along [100] and are flat, bridged by Ti(2) centres to form a Kagome net, as shown in Figure 3–7(a). The net is not strictly flat, so that the interplanar Ti(2)–Ti2 distance is ~0.2 Å shorter than the Ti(1)–Ti(1) distance for both compounds (Figure 3–7(b)). A possible explanation for this is the influence of the *RE* atom on the *X* centres. The proximity of the *RE* draws the two *X*(1) centres together and pushes the Ti(2) centres into the layer. This causes the two Ti(2) centres to become slightly closer together, as the Ti(2) centre on the other side of the layer is also pushed in. More drastic distortion from *RE* influence is likely kept from occurring by the strength of the Sb–Ti interaction.

Throughout all of this analysis, the presence of Sn has not been considered, which substitutes for Sb for up to 10%. Starting from the assumption that each tin will be –4 it can been seen that either all the Ti centres would have a slightly greater positive charge than +3, or that mixed valency will arise with two of 15 centres being Ti^{4+}.

Conclusions

RE$Ti_3(Sn_{0.1}Sb_{0.9})_4$ (*RE* = Nd, Sm) is a new layered pseudoquaternary phase that may contain a Ti^{3+} centre. Exploratory efforts show evidence that the *RE*Ti_3Sb_4 end member can be synthesised rationally for *RE* = La, Ce, Pr and Sm, but not in good yield. Variable composition studies of *RE*$Ti_3(Sn_xSb_{1-x})_4$ indicate that there is a narrow phase width of $0 \leq x \leq 0.2$. Calculations of the electronic structure would shed light on the nature of the bonding such as the Ti–Ti interactions. Future directions include the optimization of synthetic conditions to improve yields and to obtain samples for property measurements.

Table 3–1. Reaction conditions and results of exploratory $RETi_3Sb_4$ (RE = La, Ce, Pr, Nd, Sm, Gd) reactions.[a] Where indicated as a product, the $RETi_3Sb_4$ phase was detected at low yields (~5%).

Trial	Loading stoichiometries	Reaction products
1[b]	$RETi_3Sb_4$	RE_3TiSb_5 (major) RE = La, Ce, Pr, Sm $RETi_3Sb_4$ for RE = La, Ce, Pr
2[c]	$RETi_3Sb_4$ [d] 25% excess Sb as flux	TiSb and elemental Sb
3[c]	$RETi_3Sb_4$ [d] 5% excess Sb as flux	RE_3TiSb_5 (major), RE = La, Ce, Pr, Nd $RETi_3Sb_4$, for RE = La, Ce, Nd
4[c]	$SmTi_3Sb_4$[e] 25% excess Sb as a flux	T = 600 °C: Sm_3TiSb_5 (major) + SmSb + Ti_2Sb T = 700 °C: Sm_3TiSb_5 (major) + SmSb T = 800 °C: Ti_2Sb (major) + $SmTi_3Sb_4$
5[c]	$SmTi_3Sn_4$[d] 50% excess Sn as a flux	elemental tin
6[b]	$SmTi_3(Sn_xSb_{1-x})_4$ x = 0, 0.2, 0.4, 0.6, 0.8, 1	x = 0: Sm_3TiSb_5 + SmSb + $SmTi_3Sb_4$ x = 0.2: Sn + SmSb + $SmTi_3Sb_4$ x = 0.4 to 1.0: Sn + SmSb
7[c]	$NdTi_3Sb_4$[f]	binaries
8[c]	$NdTi_3Sn_4$[f]	binaries

[a] All products were characterized by XRD, except in trial 2, where EDX analysis was performed.

[b] Arc melting reaction.

[c] Reaction of elemental powders.

[d] Heated 570 °C for 1 day and 950 °C for 2 days, then immediately centrifuged.

[e] Variable temperature study. The reaction mixture was heated to T = 600, 700, 800 °C for 1 day and centrifuged while hot.

[f] Variable temperature study. The reaction mixture was heated to T = 500, 600, 700, 800 °C for 1 day and centrifuged while hot.

Table 3–2. Crystallographic data for $NdTi_3(Sn_{0.1}Sb_{0.9})_4$ and $SmTi_3(Sn_{0.1}Sb_{0.9})_4$

Formula	$NdTi_3(Sn_{0.1}Sb_{0.9})_4$	$SmTi_3(Sn_{0.1}Sb_{0.9})_4$
Formula mass (amu)	773.72	779.83
Space group	D_{2h}^{23}–*Fmmm* (No. 69)	
a (Å) [a]	5.7806(4)	5.7590(4)
b (Å) [a]	10.0846(7)	10.0686(6)
c (Å) [a]	24.2260(17)	24.1167(14)
V (Å^3)	1412.26(17)	1398.41(15)
Z	8	8
T (°C)	22	22
Diffractometer	Bruker PLATFORM/SMART - 1000 CCD	
ρ_{calc} (g cm^{-3})	7.278	7.408
Crystal dimensions (mm)	Plate, 0.23 × 0.20 × 0.10	Needle, 0.19 × 0.06 × 0.03
Radiation	Graphite monochromated Mo *K*α, λ = 0.71073 Å	
μ(Mo *K*α) (cm^{-1})	252.4	264.6
Transmission factors [b]	0.027–0.123	0.114–0.455
Scan type	ω scans (0.2 °)	
2θ limits	3° ≤ 2θ(Mo *K*α) ≤ 65°	7° ≤ 2θ(Mo *K*α) ≤ 65°
Data collected	$-8 \le h \le 8$, $-15 \le k \le 15$, $-36 \le l \le 36$	$-8 \le h \le 8$, $-15 \le k \le 14$, $-33 \le l \le 36$
No. of data collected	4119	4179
No. of unique data, including $F_o^2 < 0$	742 (R_{int} = 0.039)	732 (R_{int} = 0.040)
No. of unique data, with $F_o^2 > 2\sigma(F_o^2)$	742	713
No. of variables [c]	29	29
$R(F)$ for $F_o^2 > 2\sigma(F_o^2)$ [d]	0.0216	0.0266

$R_w(F_o^2)$ [e]	0.0531	0.0646
Goodness of fit [f]	1.378	1.287
$\Delta\rho_{max}$, $\Delta\rho_{min}$ (e Å^{-3})	1.37, –3.01	2.32, –2.44

[a] Obtained from a refinement constrained so that $\alpha = \beta = \gamma = 90°$.
[b] A numerical face-indexed absorption correction was applied, with the use of programs in the SHELXTL package (Sheldrick, G. M. *SHELXTL Version 5.1*; Bruker Analytical X-ray Systems: Madison, WI, 1997).
[c] Including an extinction coefficient.
[d] $R(F) = \Sigma\left||F_o| - |F_c|\right| / \Sigma|F_o|$.
[e] $R_w(F_o^2) = \left[\Sigma\left[w(F_o^2 - F_c^2)^2\right] / \Sigma wF_o^4\right]^{1/2}$; $w^{-1} = \left[\sigma^2(F_o^2) + (aP)^2 + bP\right]$ where $P = \left[\max(F_o^2, 0) + 2F_c^2\right]/3$. For $NdTi_3(Sn_{0.1}Sb_{0.9})_4$, $a = 0.0137$ and $b = 39.46$. For $SmTi_3(Sn_{0.1}Sb_{0.9})_4$, $a = 0.0285$ and $b = 34.38$.

[f] $GooF = \left[\Sigma\left[w(F_o^2 - F_c^2)^2\right] / (n-p)\right]^{1/2}$ where n is the number of reflections and p is the total number of parameters refined.

Table 3–3. Positional and equivalent isotropic displacement parameters for $RETi_3(Sn_{0.1}Sb_{0.9})_4$ *RE* = Nd, Sm

Atom	Wyckoff position	*x*	*y*	*z*	U_{eq} (Å^2)[a]
		$NdTi_3(Sn_{0.1}Sb_{0.9})_4$			
Nd	8*i*	0	0	0.30482(2)	0.0050(2)
Ti(1)	16*j*	1/4	1/4	0.09539(3)	0.0040(2)
Ti(2)	8*i*	0	0	0.09206(5)	0.0048(2)
X[b] (1)	16*m*	0	0.16044(3)	0.18772(1)	0.0049(1)
X[b] (2)	8*i*	0	0	0.43426(2)	0.0051(1)
X[b] (3)	8*h*	0	0.17078(5)	0	0.0060(1)
		$SmTi_3(Sn_{0.1}Sb_{0.9})_4$			
Sm	8*i*	0	0	0.30473(2)	0.0073(1)
Ti(1)	16*j*	1/4	¼	0.09598(4)	0.0059(2)
Ti(2)	8*i*	0	0	0.09236(6)	0.0066(3)
X[b] (1)	16*m*	0	0.15982(4)	0.18876(2)	0.0070(1)
X[b] (2)	8*i*	0	0	0.43361(2)	0.0071(1)
X[b] (3)	8*h*	0	0.17097(5)	0	0.0079(2)

[a] U_{eq} is defined as one-third of the trace of the orthogonalized U_{ij} tensor.
[b] *X* represents disordered crystallographic site with 10% Sn, 90% Sb.

Table 3–4. Selected interatomic distances (Å) for $RETi_3(Sn_{0.1}Sb_{0.9})_4$ (*RE* = Nd, Sm)

	$NdTi_3(Sn_{0.1}Sb_{0.9})$	$SmTi_3(Sn_{0.1}Sb_{0.9}$
RE–*X*[b](1) (×4)	3.3173 (2)	3.3023 (3)
RE–*X*[b](1) (×2)	3.4291 (4)	3.4288 (4)
RE–*X*[b](1) (×2)	3.2659 (5)	3.2265 (6)
RE–*X*[b](2) (×2)	3.1357 (6)	3.1083 (7)
RE–*RE* (×2)	3.9254 (1)	3.9063 (1)
Ti(1)–*X*[b](1) (×2)	2.8119 (11)	2.8114 (9)
Ti(1)–*X*[b](3) (×2)	2.8403 (7)	2.8397 (8)
Ti(1)–*X*[b](2) (×2)	2.9934 (3)	2.9864 (3)
Ti(2)–*X*[b](1) (×2)	2.8263 (11)	2.8275 (13)
Ti(2)–*X*[b](3) (×2)	2.8179 (11)	2.8150 (12)
Ti(2)–*X*[b](2) (×2)	2.9598 (3)	2.9468 (4)
Ti(1)–Ti(1) (×2)	2.8903 (2)	2.8795 (2)
Ti(1)–Ti(2) (×2)	2.9071 (2)	2.9011 (1)
X[b](1)–*X*[b](1)	3.2360 (7)	3.2183 (8)
X[b](2)–*X*[b](2)	3.1855 (10)	3.2020 (11)
X[b](3)–*X*[b](3)	3.3026 (5)	3.2900(5)
X[b](1)–*X*[b](1)	3.5270 (7)	3.4673 (8)

[a] At 22 °C.
[b] *X* represents disordered crystallographic site with 10% Sn, 90% Sb.

Table 3–5. Refined cell parameters for observed $RETi_3Sb_4$ phases

Trial	Compound	no. of reflection	a (Å)	b (Å)	c (Å)	V (Å^3)
1	$LaTi_3Sb_4$	6	5.80 (1)	10.18 (2)	24.92 (5)	1484 (4)
3	$LaTi_3Sb_4$	13	5.849 (7)	10.21 (1)	24.98 (3)	1500 (2)
1	$CeTi_3Sb_4$	9	5.864 (3)	10.196 (8)	24.91 (2)	1489 (1)
3	$CeTi_3Sb_4$	15	5.84 (1)	10.17 (2)	24.78(5)	1473 (3)
1	$PrTi_3Sb_4$	11	5.81 (1)	10.17 (2)	24.50 (6)	1448 (3)
3	$NdTi_3Sb_4$	6	5.794(7)	10.07(1)	24.39(2)	1423(2)
6	$SmTi_3Sb_4$	16	5.731 (9)	10.03 (1)	24.10 (3)	1386 (2)
6	$SmTi_3(Sn_{0.2}Sb_{0.8})_4$	13	5.733 (8)	10.05 (1)	24.18 (2)	1393 (2)

Table 3–6. Comparison of interatomic distances (Å) in Ti–Sb phases [a,13,14]

Compound	Sb–Sb	Sb–Ti	Ti–Ti
Ti_3Sb[13]	4.519	2.917	2.609
Ti_3Sb[13]	3.671 (4)	2.755 (3)	2.632 (11)
TiSb[13]	3.132	2.845	2.845
$TiSb_2$[14]	3.450	2.917	2.903
$NdTi_3(Sn_{0.1}Sb_{0.9})_4$	3.1855 (10) – 3.5270 (7)	2.8119 (11) – 2.9934 (3)	2.8903 (2) – 2.9071 (2)
$SmTi_3(Sn_{0.1}Sb_{0.9})_4$	3.2183(8) – 3.2900	2.8114 (9) – 2.9864 (4)	2.8795 (2) – 2.9011 (11)

[a] When interatomic distances were unavailable from literature sources, they were calculated with the program Atoms 5.1.[15]

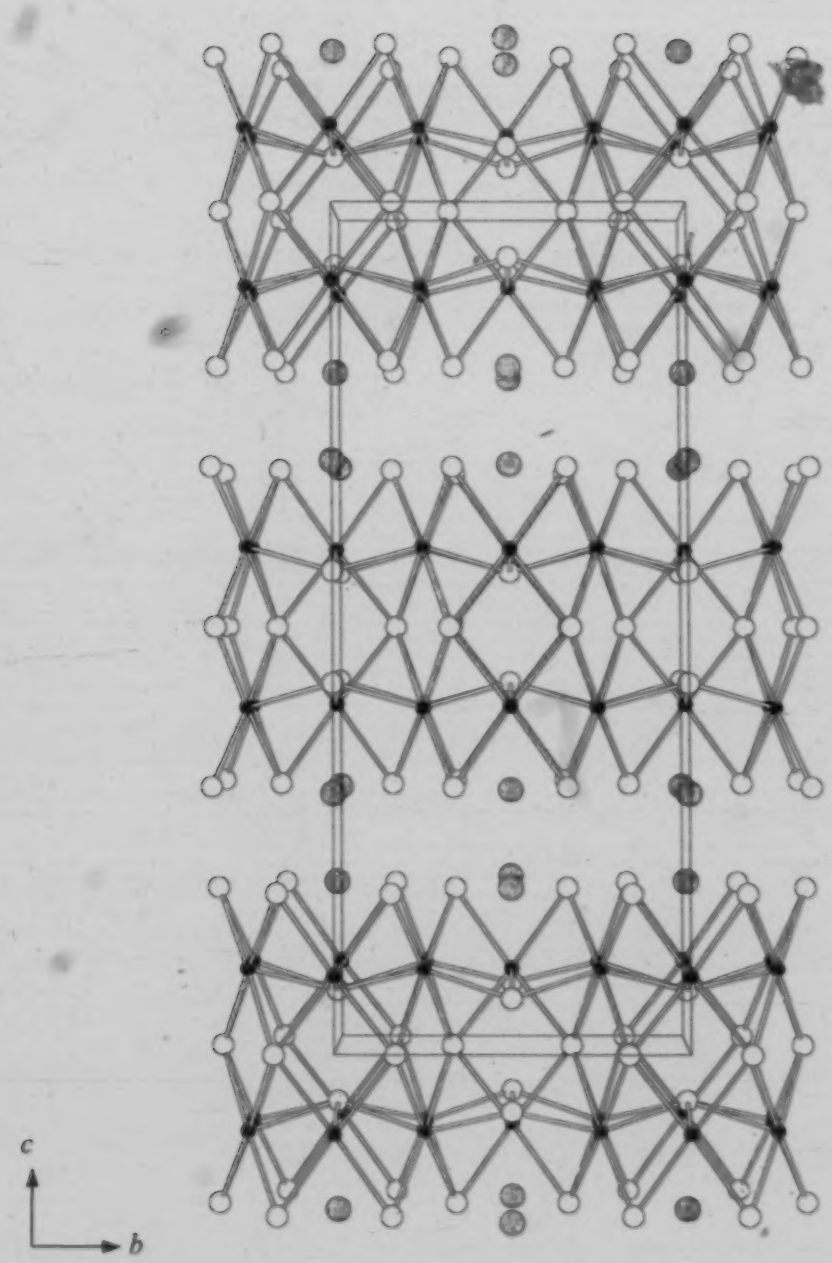

Figure 3–1. Structure of $RETi_3(X)_4$ (RE= Nd, Sm; $X = Sn_{0.1}Sb_{0.9}$) viewed down [100]. The large shaded circles are RE atoms, the small solid circles are Ti atoms, and the open circles represent $Sn_{0.1}Sb_{0.9}$.

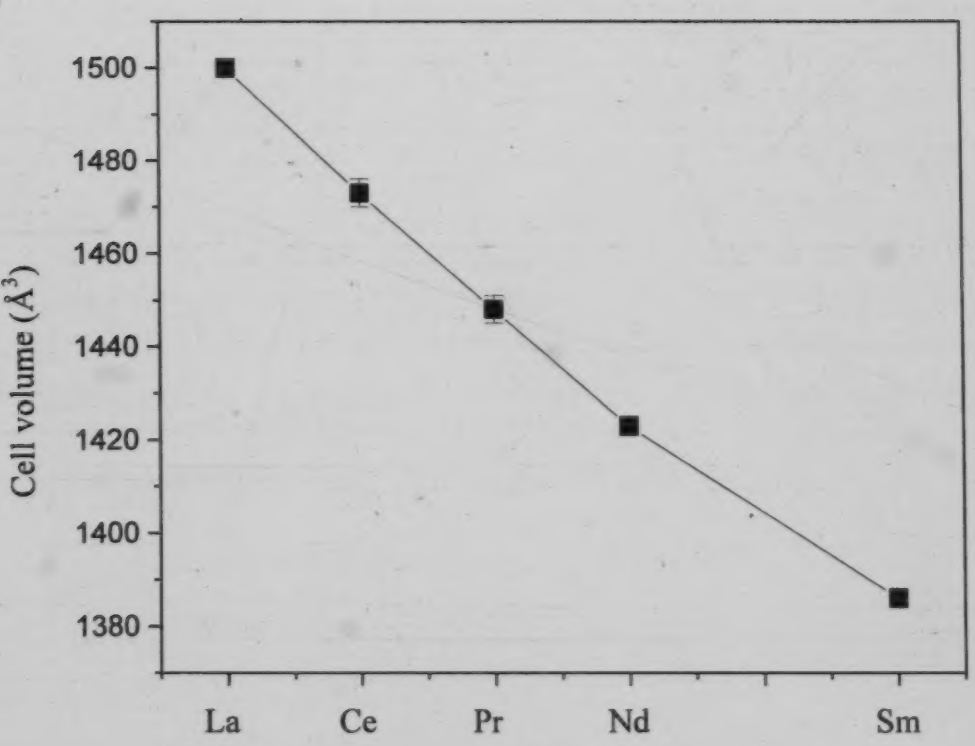

Figure 3–2. Plot of unit cell volumes vs *RE*.

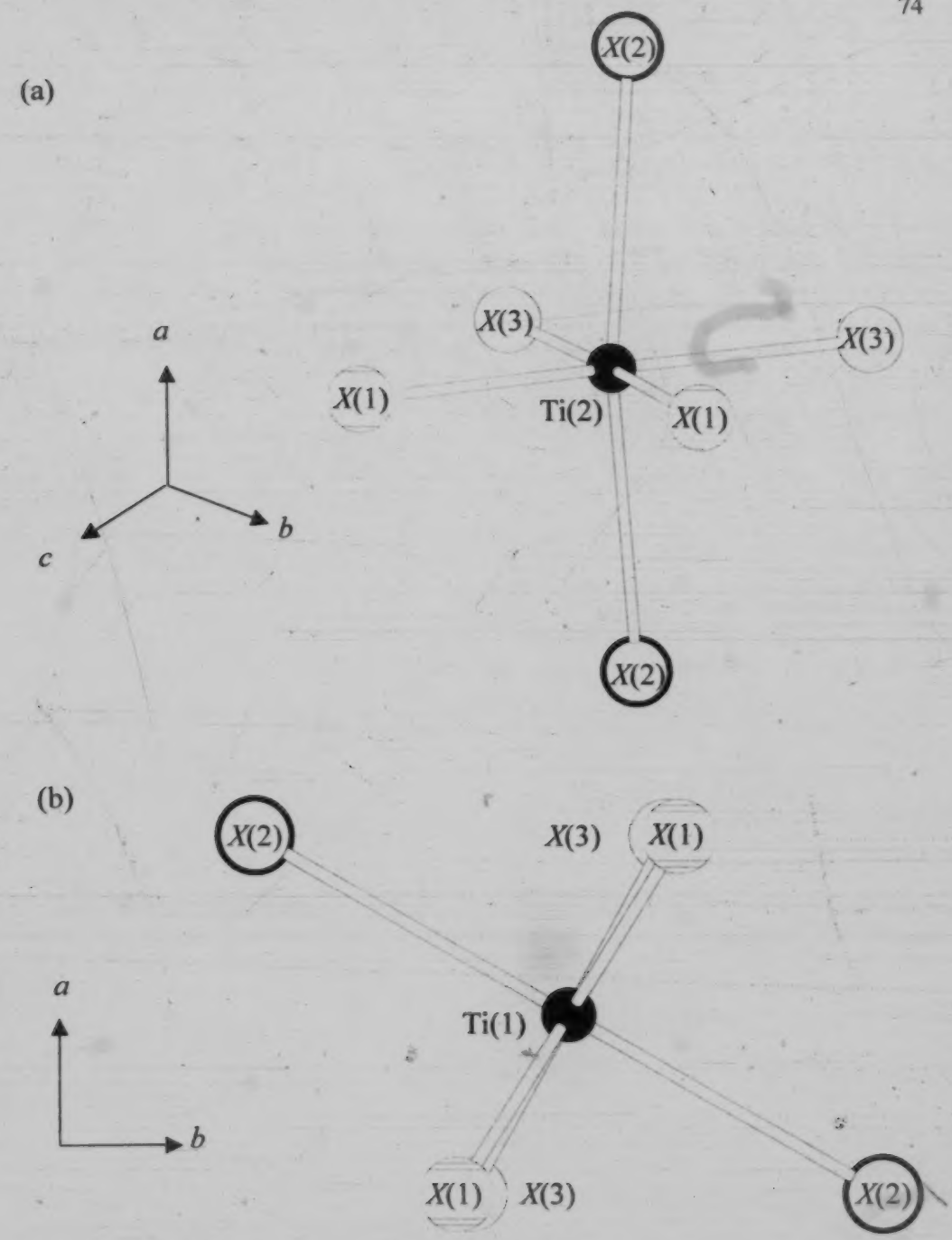

Figure 3–3. (a) type 1 octahedron, (b) type 2 octahedron. Small dark circles are Ti atoms, circles with horizontal hachure are X(1), open circles with thick rims are X(2) and the open circles are X(3).

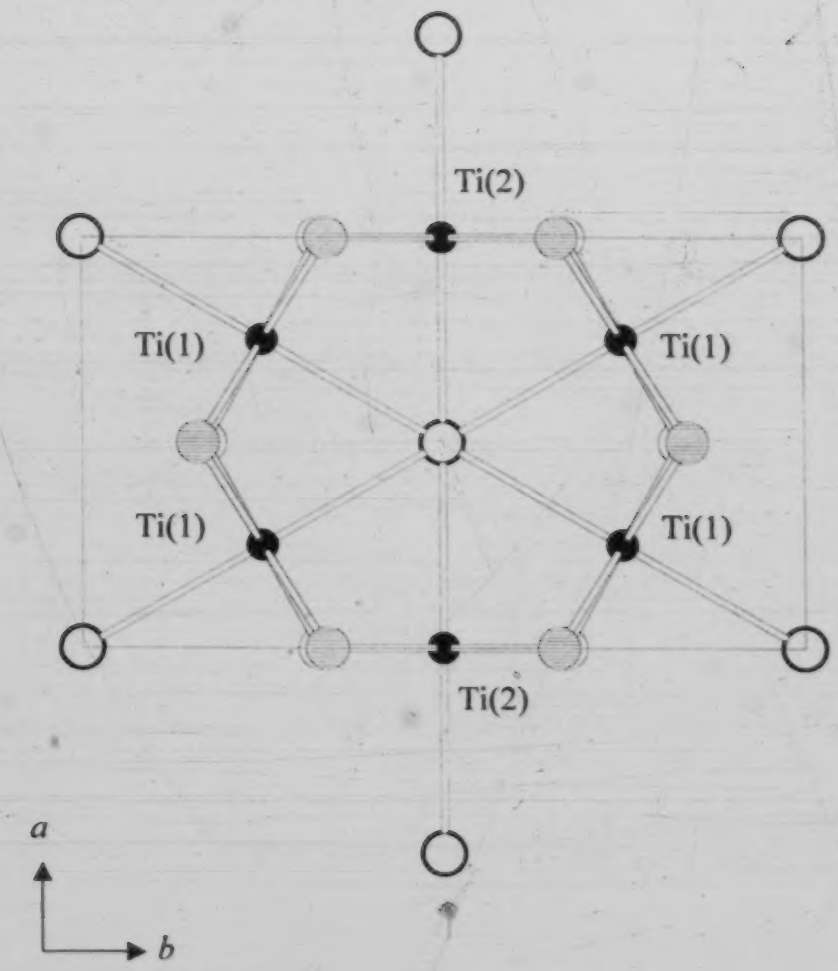

Figure 3–4. Six $TiSb_{4/6}Sb_{2/3}$ octahedra forming a pseudohexagonal arrangement. The solid black circles are the Ti atoms, circles with horizontal hachure are *X*(1), open circles with thick rims are *X*(2) and the open circles are *X*(3).

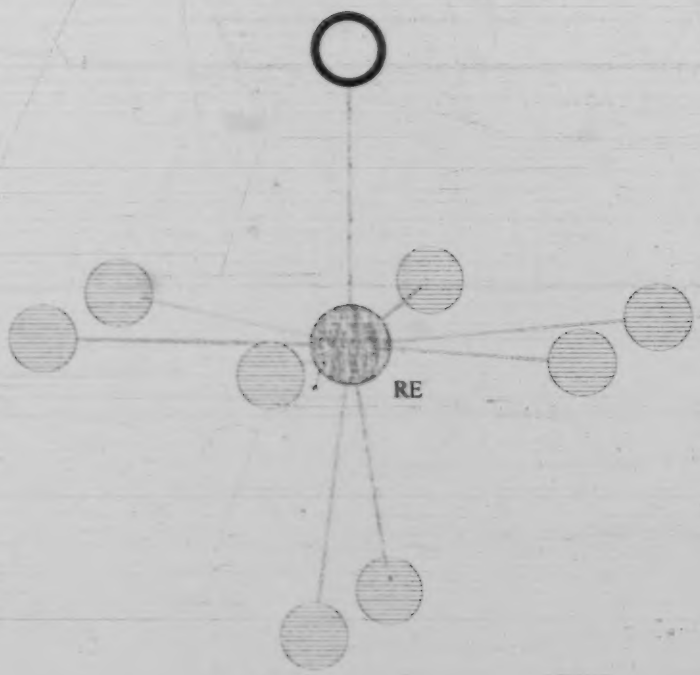

Figure 3–5. Coordination environment of the *RE* atom in $RETi_3(Sn_{0.1}Sb_{0.9})_4$ (*RE* = Nd, Sm). Circles with horizontal hachure are *X*(1) and open circles with thick rims are *X*(2).

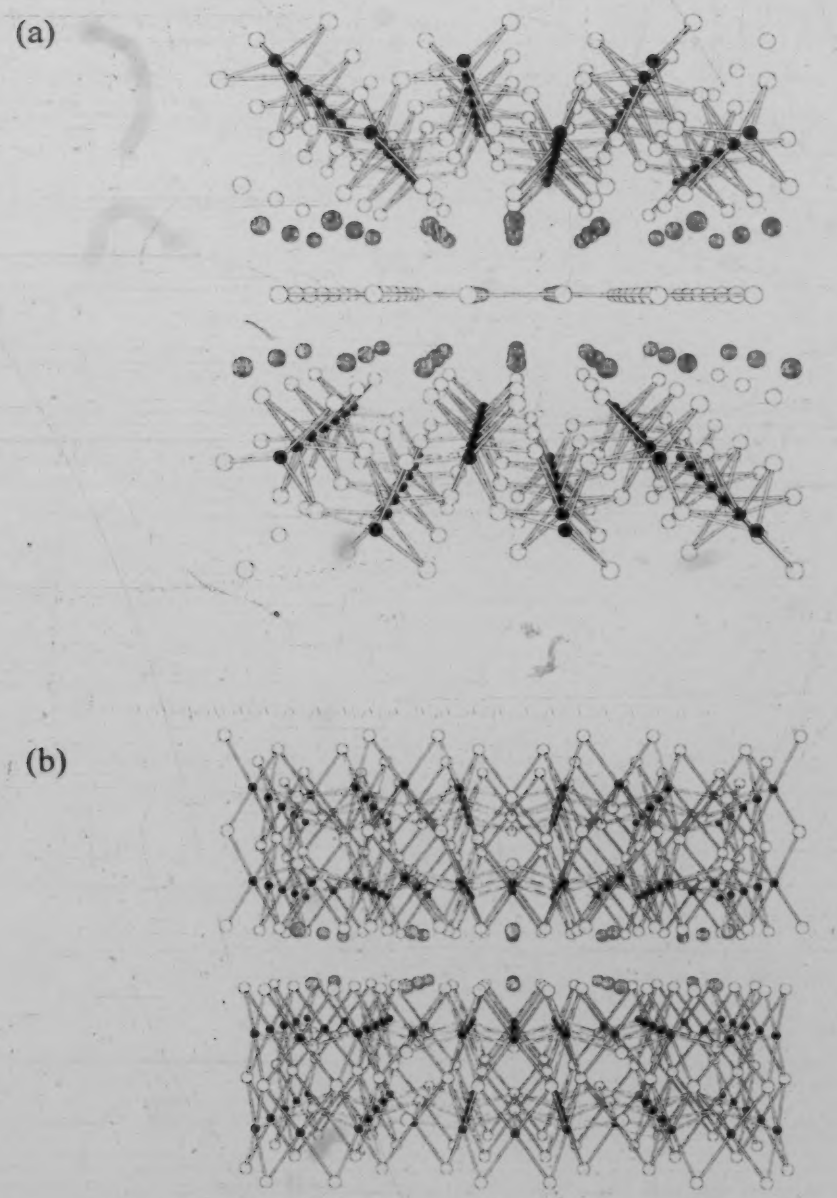

Figure 3–6. Comparison of (a) *RE*CrSb$_3$ and (b) *RE*Ti$_3$(Sn$_{0.1}$Sb$_{0.9}$)$_4$, (*RE*= Nd, Sm). Large shaded circles are *RE* atoms, the small solid circles are *M* atoms (*M* = Cr, Ti), and the open circles are Sb or Sn atoms.

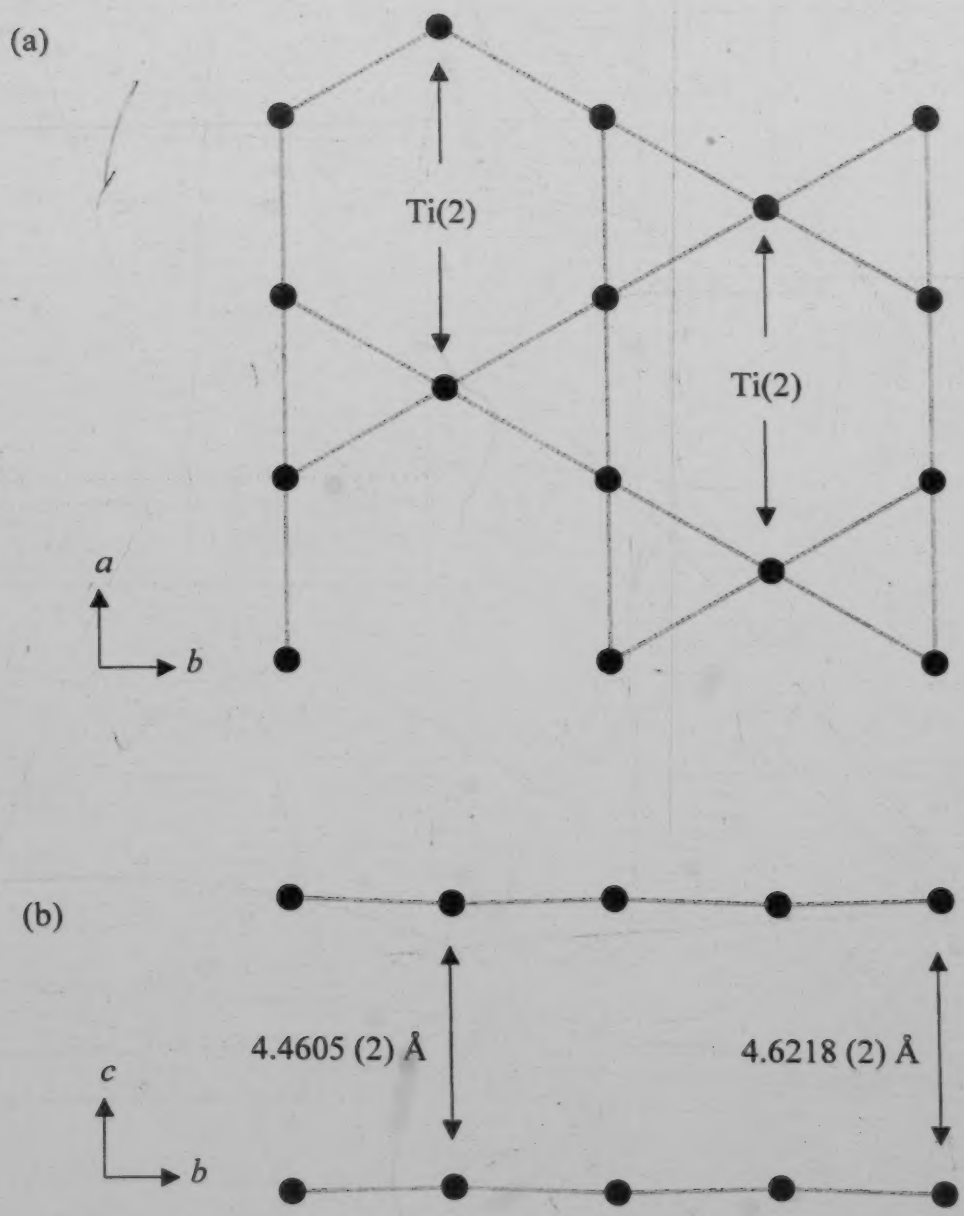

Figure 3–7. Arrangement of Ti atoms in $NdTi_3(Sn_{0.1}Sb_{0.9})_4$. The Ti(1) and Ti(2) inter layer distances for $SmTi_3(Sn_{0.1}Sb_{0.9})_4$ are 4.455 (2) Å and 4.629 (2) Å respectively. Ti(2) centers are indicated in (a), all other centers are Ti(1).

References

(1) Karla, I.; Peirre, J.; Skolozdra, R. V. *J. Alloys Compd*, **1998**, *265*, 42-48

(2) Brylak, M.; Jeitschkoy, S. *Z. Naturforsch. B: Chem. Sci.*, **1995**, *50*, 899-904.

(3) Ferguson, M.J.; Hushagen, R.W.; Mar, A. *J. Alloys Compd.*, **1997**, *249*, 191-198.

(4) Jackson, D.D.; Fisk, Z. *J. Magn. Magn. Mater.*, **2003**, *256*, 106-116.

(5) Deakin, L.; Ferguson, M.J.; Mar, A.; Greedan, J.E.; Wills, A.S. *Chem. Mater.*, **2001**, *13*, 1407-1412.

(6) Bolloré, G.; Ferguson, M.J.; Hushagen, R.W.; Mar, A. *Chem. Mater.*, **1995**, *7*, 2229-2231.

(7) Sheldrick, G.M. *SHELXTL*, version 5.1; Bruker Analytical X-ray Systems, Inc.; Madison, WI, 1997.

(8) Donohue, J. *The Structures of the Elements*; Wiley: New York, 1974.

(9) Eisenmann, B.; May, N.; Mueller, W.; Scaefer, H. *Z. Naturforsch. B: Chem. Sci.*, **1972**, *27*, 1155-1157.

(10) Ban, Z.; Sikirica, M. *Acta Crys.*, **1965**, *18*, 594-599.

(11) Yarmolyuk, Y.P.; Sikirica, M.; Aksel'red, L.G.; Lysenko, L.A.; Gladyshevskii, E.L. *Kristallographiia*, **1982**, *27*, 1090-1093.

(12) Teatum, E.; Gschneidner, K.; & Waber, J. *Compilation of calculated data useful in predicting metallurgical behaviour of the elements in binary alloy systems*, LA-2345, Los Alamos Scientific Laboratory, 1960.

(13) Kjekshus, A.; Grønvold, F.; Thorbjørnsen, J. *Acta Chemica Scandinavica* **1962**, *16*, 1493-1510.

(14) Hainga, E.E.; Damsma, H.; Hokkeling, P. *J. Less Com. Met.*, **1972**, *27*, 169-186.

(15) Dowty, E. *Atoms*, version 5.1 Beta, Shape Software, 1999.

Conclusion

As in Chapter 3, for the purposes of the discussion herein, *X* will be used to represent $Sn_{0.1}Sb_{0.9}$. Two new compounds $RETi_3(Sn_{0.1}Sb_{0.9})_4$ (*RE* = Nd, Sm) were isolated from reactions of the elements intended to produce the respective RE_3TiSb_5 (*RE* = Nd, Sm) compounds. The crystal structure of both members was determined and found to be composed of layers of face- and edge-sharing $TiSb_{4/6}Sb_{2/3}$ octahedra. Other structural points of interest are Ti–Ti metal bonding and the possible presence of a Ti^{3+} centre. The range of tin substitution was explored with the Sm phase $SmTi_3(Sn_xSb_{1-x})_4$, and was found to be narrow, $0 \leq x \leq 0.2$. A Sn-free phase was produced, but the reactions yielded low amounts of the target compounds. The extent of *RE* substitution was explored and the Sn-free phase was found to include *RE* = La–Nd, Sm. Synthetic optimization indicates that the phase requires a reaction temperature of 700 °C.

The series RE_3TiSb_5 (*RE* = La–Nd, Sm) have undergone electronic characterization by our group prior to this work. The crystal structure possesses low-dimensional features that are manifested as isolated linear antimony chains and $TiSb_{6/2}$ face-sharing octahedra. Extended Hückel band structure calculations of the La_3TiSb_5 member demonstrated the potential for a superconductive phase. Previous work had characterised the members between 20 and 300 K, but no superconducting phase was uncovered. The results of the electronic and magnetic properties between 2 and 300 K of family RE_3TiSb_5 (*RE* = La–Nd, Sm) were presented in chapter 2. Both the La and Ce members were found to superconducting (T_C ~4.0 K), and the Nd member is also thought to be a superconductor. Both Pr and Sm members did not reveal a superconducting phase; the Sm member data indicated a magnetic ordering onset at 15 K, which is

probably responsible for suppression of a superconducting phase. The remaining members of the series were characterized by X-ray diffraction to allow a comparative study of the band structures of all members. The differences in the band structures of the various members are small. This indicates that the nature of the rare-earth element may have a significant role, or that the appearance of a superconducting phase is somehow sensitive to the contraction of the unit cell.

The characterization of the series RE_3TiSb_5 (RE = La–Nd, Sm) and the discovery of the phase $RETi_3(Sn_{0.1}Sb_{0.9})_4$ are significant as they expand on the sparse information known on rare-earth transition-metal antimonides, with the majority of publications from our group. In addition, most work in this area from other groups focuses on structural aspects; chapter two represents one of the first few in-depth characterization studies of the rare-earth early-transition-metal antimonides. It is somewhat surprising that, in the course of attempts to prepare members of the RE_3TiSb_5 phase, the $RETi_3X_4$ phase was uncovered. This phase is unique among layered rare-earth transition metal ternary antimonides in that the rare-earth atoms are positioned on the anionic layer rather then forming their own distinct layer. This phase is also of interest because of the Ti–Ti bonding and the possible presence of a Ti^{3+} centre, raising the possibility of additional magnetic and electronic behaviour.

Both of these low dimensional phases have a common structural feature, namely face-sharing $TiSb_6$ octahedra, which are also found in the $REMSb_3$ (M = V, Cr) phase. Despite the similar coordination polyhedra, the Ti–Ti distances in the $RETi_3X_4$ are significantly longer then those found in the RE_3TiSb_5 phase, and the octahedra are not regular. The differences in the order of the dimensionality would also have an impact on

the properties of the RETi$_3X_4$ phase. Speculation of a metallic character based on the extended network is not unreasonable, as is expected anisotropy due to the layered nature of the phase.

The RETi$_3X_4$ phase can be related back to the RE_3TiSb$_5$ phase by manipulating the Ti$_3X_4$ framework as shown in Figure 4–1. The similarity between the two structures raises the question as to whether or not one phase is the precursor for the other. It is more likely however that the two phases simply represent minima on the energy landscape. Although we have found the RE_3TiSb$_5$ phase to form relatively more easily than the RETi$_3X_4$ phase, the methodology employed could be favouring the formation of one product over the other.

Future Directions

The compounds RE_3TiSb$_5$ (RE = La, Ce, Pr, Nd, Sm) require additional characterization, mainly to determine the nature of the magnetic ordering of the 4f electrons. Efforts have been made to expand the phase by substituting As and Bi for Sb using standard reaction conditions, but so far these efforts have been unsuccessful. Additional studies should examine the effect of the RE content on the suppression of the superconducting effect in both the Pr and Sm members by gradually substituting with La. A larger goal would be to extend the phase to include other transition metals. We are currently measuring both the Zr and Hf members of the RE_3MSb$_5$ phase; preliminary data indicate that Zr series contains a superconducting phase. The RETi$_3$(Sn$_{0.1}$Sb$_{0.9}$) phase still requires substantial investigation, both in syntheses and characterization. Initial efforts should focus on preparing the phase free of Sn. Further experiments will involve extending the phase to include other transition metals. Theoretical calculations may

assist in understanding the nature of the bonding in the structure, with specific interest in the bonding between Ti atoms.

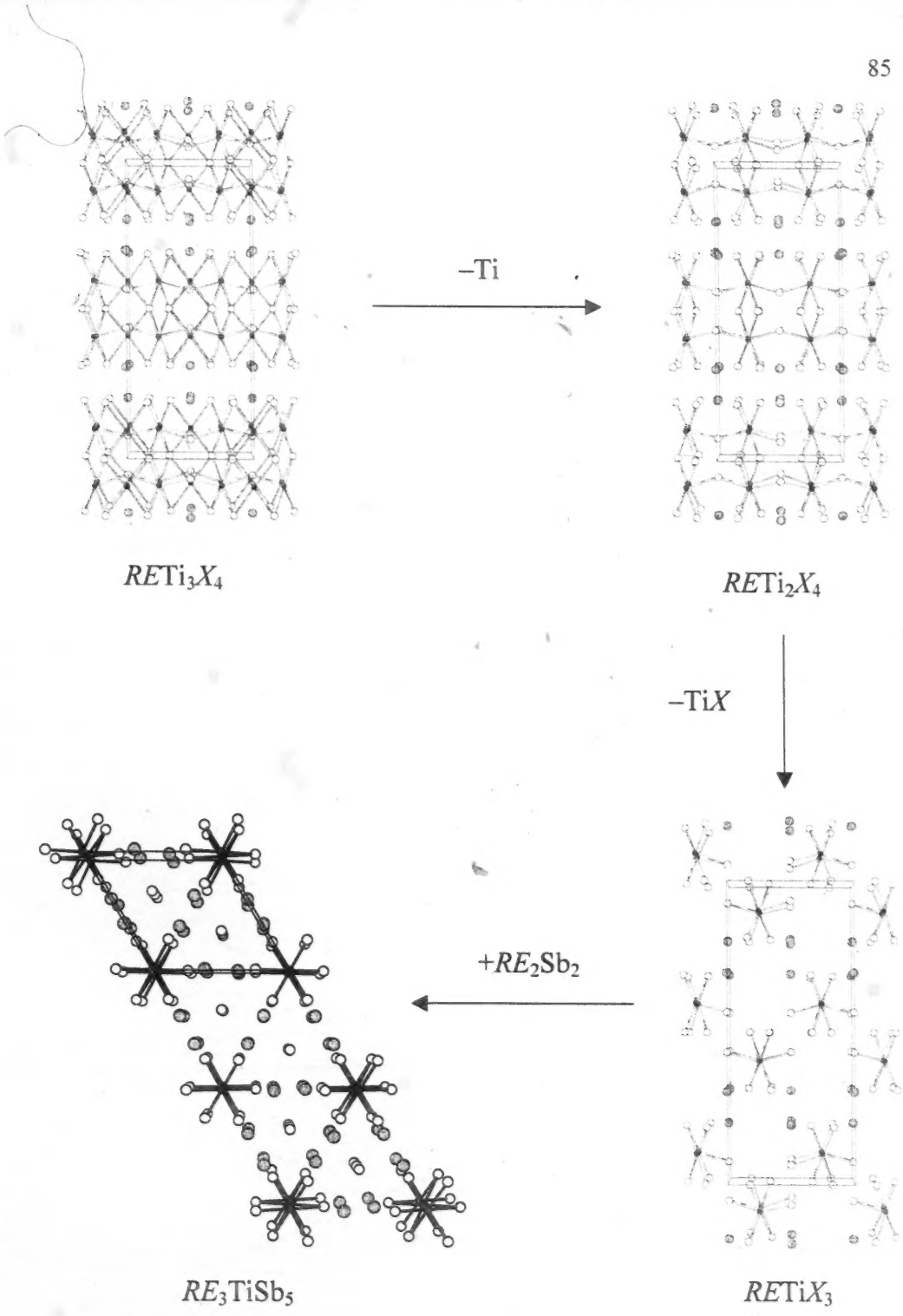

Figure 4–1. Hypothetical transformation of RETi$_3X_4$ phase to the RE_3TiSb$_5$ phase. X = Sn$_{0.1}$Sb$_{0.9}$. Large shaded circles are RE atoms, the small solid circles are Ti atoms and the open circles are Sb or Sn atoms.

Appendix

Table A–1. Anisotropic displacement parameters ($Å^2$) for Ce_3TiSb_5, Pr_3TiSb_5, Nd_3TiSb_5 and Sm_3TiSb_5 for data collections at 22 °C [a]

Atom	U_{11}	U_{22}	U_{33}	U_{12}	U_{13}	U_{23}
			Ce_3TiSb_5			
Ce	0.0082(3)	0.0092(4)	0.0071(4)	0.0046(2)	0	0
Ti	0.008(1)	0.008(1)	0.009(2)	0.0038(6)	0	0
Sb(1)	0.0074(3)	0.0084(4)	0.0080(4)	0.0042(2)	0	0
Sb(2)	0.0081(3)	0.0081(3)	0.0078(5)	0.0040(2)	0	0
			Pr_3TiSb_5			
Pr	0.0099(2)	0.0112(2)	0.0085(2)	0.0056(1)	0	0
Ti	0.0097(6)	0.0097(6)	0.009(1)	0.0048(3)	0	0
Sb(1)	0.0092(2)	0.0101(2)	0.0088(2)	0.0051(1)	0	0
Sb(2)	0.0098(2)	0.0098(2)	0.0092(3)	0.0049(1)	0	0
			Nd_3TiSb_5			
Nd	0.0114(2)	0.0129(3)	0.0076(3)	0.0064(1)	0	0
Ti	0.0109(7)	0.0109(7)	0.0087(11)	0.0055(4)	0	0
Sb(1)	0.0104(2)	0.0116(3)	0.0080(3)	0.0058(1)	0	0
Sb(2)	0.0113(2)	0.0113(3)	0.0084(3)	0.0056(1)	0	0
			Sm_3TiSb_5			
Sm	0.0096(3)	0.0106(4)	0.0068(3)	0.0053(2)	0	0
Ti	0.008(1)	0.008(1)	0.007(2)	0.0042(6)	0	0
Sb(1)	0.0086(3)	0.0096(4)	0.0067(4)	0.0048(2)	0	0
Sb(2)	0.0090(4)	0.0090(4)	0.0067(5)	0.0045(2)	0	0

[a] The form of the anisotropic displacement parameter is:

$$\exp\left[-2\pi^2\left(h^2a^{*2}U_{11}+k^2b^{*2}U_{22}+l^2c^{*2}U_{33}+2hka^*b^*U_{12}+2hla^*c^*U_{13}+2klb^*c^*U_{23}\right)\right]$$

Table A–2. Anisotropic displacement parameters ($Å^2$) for $NdTi_3X_4$ and $SmTi_3X_4$ (X = $Sn_{0.1}Sb_{0.9}$) for data collections at 22°C [a]

Atom	U_{11}	U_{22}	U_{33}	U_{12}	U_{13}	U_{23}
			$NdTi_3X_4$			
Nd	0.0047(2)	0.0060(2)	0.0042(2)	0	0	0
Ti(1)	0.0041(4)	0.0045(4)	0.0034(4)	-0.0003(3)	0	0
Ti(2)	0.0056(5)	0.0043(5)	0.0045(5)	0	0	0
X(1)	0.0057(2)	0.0052(2)	0.0038(2)	0	0	0.0002(1)
X(2)	0.0046(2)	0.0049(2)	0.0059(2)	0	0	0
X(3)	0.0080(2)	0.0075(2)	0.0024(2)	0	0	0
			$SmTi_3X_4$			
Sm	0.0078(2)	0.0068(2)	0.0073(2)	0	0	0
Ti(1)	0.0062(4)	0.0046(4)	0.0069(4)	-0.0005(3)	0	0
Ti(2)	0.0076(6)	0.0047(6)	0.0074(6)	0	0	0
X(1)	0.0085(2)	0.0055(2)	0.0069(2)	0	0	0.0001(1)
X(2)	0.0071(2)	0.0053(2)	0.0091(2)	0	0	0
X(3)	0.0103(3)	0.0074(2)	0.0059(2)	0	0	0

[a] The form of the anisotropic displacement parameter is:

$$\exp\left[-2\pi^2\left(h^2a^{*2}U_{11}+k^2b^{*2}U_{22}+l^2c^{*2}U_{33}+2hka^*b^*U_{12}+2hla^*c^*U_{13}+2klb^*c^*U_{23}\right)\right]$$

Table A–3. X-ray powder diffraction data for trial 1 $LaTi_3Sb_4$ [a]

hkl	d_{obs} (Å)	d_{calc} (Å)	I/I_0 [b]
2 0 0	2.946	2.945	14
1 1 7	2.919	2.922	73
1 3 1	2.920	2.922	21
1 3 3	2.771	2.765	16
1 3 5	2.532	2.537	100
1 3 15	1.446	1.445	26

[a] The orthorhombic cell parameters refined from the powder pattern, obtained on a Guinier camera at room temperature, are: $a = 5.89(1)$ Å, $b = 10.18(2)$ Å, $c = 24.92(5)$ Å, and $V = 1484(4)$ Å^3.

[b] The intensities were calculated based on positional parameters from the crystal structure of $SmTi_3(Sn_{0.1}Sb_{0.9})_4$ with the use of the program LAZY-PULVERIX (Yvon, K.; Jeitschko, W.; Parthé, E. *J. Appl. Crystallogr.* **1977**, *10*, 73).

Table A–4. X-ray powder diffraction data for trial 3 $LaTi_3Sb_4$ [a]

hkl	d_{obs} (Å)	d_{calc} (Å)	I/I_0 [b]
2 0 0	2.945	2.938	14
1 1 7	2.924	2.918	73
1 3 1	2.924	2.918	21
1 3 3	2.776	2.771	16
1 3 5	2.536	2.535	100
2 0 8	2.142	2.146	10
1 3 11	1.798	1.800	22
3 3 1	1.696	1.698	17
3 3 5	1.609	1.612	28
2 6 0	1.472	1.474	15
1 3 15	1.449	1.449	26
3 3 11	1.361	1.360	11
3 3 15	1.190	1.189	19

[a] The orthorhombic cell parameters refined from the powder pattern, obtained on a Guinier camera at room temperature, are: a = 5.899(7) Å, b = 10.20(1) Å, c = 24.98(3) Å, and V = 1500(2) Å^3.

[b] The intensities were calculated based on positional parameters from the crystal structure of $SmTi_3(Sn_{0.1}Sb_{0.9})_{43}$ with the use of the program LAZY-PULVERIX (Yvon, K.; Jeitschko, W.; Parthé, E. *J. Appl. Crystallogr.* **1977**, *10*, 73).

Table A–5. X-ray powder diffraction data for trial 1 $CeTi_3Sb_4$ [a]

hkl	d_{obs} (Å)	d_{calc} (Å)	I/I_0 [b]
2 0 0	2.932	2.930	14
1 3 1	2.920	2.918	73
1 1 7	2.915	2.918	21
1 3 3	2.772	2.773	16
1 3 5	2.532	2.532	100
2 2 6	2.168	2.169	28
2 0 8	2.134	2.133	10
3 3 1	1.690	1.691	17
1 3 15	1.446	1.445	26

[a] The orthorhombic cell parameters refined from the powder pattern, obtained on a Guinier camera at room temperature, are: a = 5.864(3) Å, b = 10.196(8) Å, c = 24.91(2) Å, and V = 1489(1) Å^3.

[b] The intensities were calculated based on positional parameters from the crystal structure of $SmTi_3(Sn_{0.1}Sb_{0.9})_4$ with the use of the program LAZY-PULVERIX (Yvon, K.; Jeitschko, W.; Parthé, E. *J. Appl. Crystallogr.* **1977**, *10*, 73).

Table A–6. X-ray powder diffraction data for trial 3 $CeTi_3Sb_4$ [a]

hkl	d_{obs} (Å)	d_{calc} (Å)	I/I_0 [b]
2 0 0	2.921	2.913	14
1 3 1	2.913	2.913	73
1 1 7	2.902	2.900	21
1 3 3	2.764	2.769	16
1 3 5	2.524	2.5522	100
2 2 6	2.160	2.1151	27
2 0 8	2.125	2.125	10
1 3 11	1.787	1.784	22
3 3 1	1.685	1.691	17
3 3 5	1.599	1.599	28
2 6 0	1.466	1.469	15
1 3 15	1.439	1.443	26
3 3 11	1.351	1.354	11
2 6 8	1.325	1.321	10
2 6 10	1.262	1.262	18

[a] The orthorhombic cell parameters refined from the powder pattern, obtained on a Guinier camera at room temperature, are: a = 5.84(1) Å, b = 10.17(2) Å, c = 24.78(5) Å, and V = 1473(3) Å^3.

[b] The intensities were calculated based on positional parameters from the crystal structure of $SmTi_3(Sn_{0.1}Sb_{0.9})_4$ with the use of the program LAZY-PULVERIX (Yvon, K.; Jeitschko, W.; Parthé, E. *J. Appl. Crystallogr.* **1977**, *10*, 73).

Table A–7. X-ray powder diffraction data for trial 1 $PrTi_3Sb_4$ [a]

hkl	d_{obs} (Å)	d_{calc} (Å)	I/I_0 [b]
2 0 0	2.906	2.910	14
1 3 1	2.908	2.901	72
1 3 3	2.757	2.764	17
1 3 5	2.514	2.517	100
2 2 6	2.146	2.144	27
1 3 11	1.773	1.780	22
3 3 1	1.678	1.679	16
3 3 5	1.591	1.594	28
2 6 0	1.464	1.463	15
1 3 15	1.426	1.425	26
3 3 11	1.342	1.338	11

[a] The orthorhombic cell parameters refined from the powder pattern, obtained on a Guinier camera at room temperature, are: $a = 5.81(1)$ Å, $b = 10.17(2)$ Å, $c = 24.50(6)$ Å, and $V = 1448(3)$ Å^3.

[b] The intensities were calculated based on positional parameters from the crystal structure of $SmTi_3(Sn_{0.1}Sb_{0.9})_4$ with the use of the program LAZY-PULVERIX (Yvon, K.; Jeitschko, W.; Parthé, E. *J. Appl. Crystallogr.* **1977**, *10*, 73).

Table A–8. X-ray powder diffraction data for Trial 1 $NdTi_3Sb_4$ [a]

hkl	d_{obs} (Å)	d_{calc} (Å)	I/I_0 [b]
0 0 8	3.049	3.048	25
2 0 0	2.896	2.897	56
1 1 7	2.867	2.863	23
1 3 5	2.498	2.496	100
0 0 10	2.436	2.439	26
0 6 0	1.678	1.679	12

[a] The orthorhombic cell parameters refined from the powder pattern, obtained on a Guinier camera at room temperature, are: a = 5.794 (7) Å, b = 10.07 (1) Å, c = 24.39(2) Å, and V = 1423(2) Å^3.

[b] The intensities were calculated based on positional parameters from the crystal structure of $NdTi_3(Sn_{0.1}Sb_{0.9})_4$ with the use of the program LAZY-PULVERIX (Yvon, K.; Jeitschko, W.; Parthé, E. *J. Appl. Crystallogr.* **1977**, *10*, 73).

Table A–9. X-ray powder diffraction data for trial 6 $SmTi_3Sb_4$ [a]

hkl	d_{obs} (Å)	d_{calc} (Å)	I/I_0 [b]
1 3 1	2.868	2.863	72
2 0 0	2.865	2.863	14
1 1 7	2.832	2.826	22
1 3 3	2.782	2.720	17
1 3 5	2.478	2.471	100
0 0 10	2.410	2.409	7
1 1 9	2.358	2.354	7
2 0 6	2.333	2.330	8
1 3 7	2.213	2.214	9
0 4 6	2.128	2.127	7
2 0 8	2.077	2.070	10
1 1 11	2.005	2.008	6
2 0 10	1.844	1.852	5
1 3 11	1.746	1.750	22
3 3 5	1.568	1.572	28
2 6 0	1.444	1.445	15

[a] The orthorhombic cell parameters refined from the powder pattern, obtained on a Guinier camera at room temperature, are: a = 5.731(9) Å, b = 10.03(1) Å, c = 24.10(3) Å, and V = 1386(2) Å^3.

[b] The intensities were calculated based on positional parameters from the crystal structure of $SmTi_3(Sn_{0.1}Sb_{0.9})_4$ with the use of the program LAZY-PULVERIX (Yvon, K.; Jeitschko, W.; Parthé, E. *J. Appl. Crystallogr.* **1977**, *10*, 73).

Table A–10. X-ray powder diffraction data for trial 6 $SmTi_3(Sn_{0.2}Sb_{0.8})_4$ [a]

hkl	d_{obs} (Å)	d_{calc} (Å)	I/I_0 [b]
0 0 8	3.023	3.024	7
1 3 1	2.871	2.866	72
1 1 7	2.839	2.836	22
1 3 3	2.722	2.725	17
1 3 5	2.482	2.483	100
0 0 10	2.418	2.419	7
2 2 4	2.302	2.303	9
1 3 7	2.218	2.222	9
0 4 6	2.132	2.135	7
2 2 6	2.118	2.115	26
2 0 8	2.080	2.085	10
1 3 11	1.750	1.746	22
3 3 5	1.570	1.569	28

[a] The orthorhombic cell parameters refined from the powder pattern, obtained on a Guinier camera at room temperature, are: a = 5.733(8) Å, b = 10.05(1) Å, c = 24.18(3) Å, and V = 1393(2) Å^3.

[b] The intensities were calculated based on positional parameters from the crystal structure of $SmTi_3(Sn_{0.1}Sb_{0.9})_4$ with the use of the program LAZY-PULVERIX (Yvon, K.; Jeitschko, W.; Parthé, E. *J. Appl. Crystallogr.* **1977**, *10*, 73).